


ENHANCED RECEIVER FUNCTION IMAGING OF CRUSTAL STRUCTURES USING SYMMETRIC AUTOENCODERS

A PREPRINT

 **T. Rengneichuong Koireng**
Centre for Earth Sciences
Indian Institute of Science
Bengaluru, India 560012
tienterk@iisc.ac.in

 **Pawan Bharadwaj**
Centre for Earth Sciences
Indian Institute of Science
Bengaluru, India 560012
pawan@iisc.ac.in

November 22, 2024

ABSTRACT

The receiver-function (RF) technique aims to recover receiver-side crustal and mantle structures by deconvolving either the radial or transverse component with the vertical component seismogram. Analysis of the variations of RFs along backazimuth and slowness is the key in determining the geometry and anisotropic properties of the crustal layers. Nonetheless, pseudorandom *nuisance effects*, influenced by the unknown earthquake source signature and seismic noise, are produced by the deconvolution process and obstruct precise comparisons of RFs across different backazimuths. Various methods such as weighted stacking, sparsity-induced transform and supervised denoising neural-network have been developed to reduce the nuisance effects. However, the common assumption of the nuisance effects as random Gaussian proves inadequate. Supervised denoising neural-network struggles to generalize effectively in intricate tectonic environments like subduction zones. In this study, we take an unsupervised approach where a network-based representation of a group of RFs with similar raypaths, enables disentanglement of the coherent crustal effects from the RF-specific nuisance effects. The representation learning task is performed using symmetric autoencoders (SymAE). We show that SymAE successfully produces virtual RFs that predominantly capture coherent crustal effects from the RFs within the group, while reducing unwanted nuisance effects. Our method was applied to synthetic RFs that were contaminated with nuisance effects, which are derived from the real data. The generated virtual RFs (both radial and transverse) in this case exhibit superior quality and accurately match the true synthetic RFs — our method outperforms bin-wise linear stacking and phase-weighted stacking methods. When employed with real data from the Cascadia Subduction Zone, our approach produced enhanced radial and transverse RFs. Additionally, it facilitated a clear interpretation of a dual-layer subducting slab. We also provided sanity checks to verify the accuracy of the network-derived virtual RFs. One major advantage of our method is its ability to utilize all available earthquakes, irrespective of their signal quality, thereby enhancing reproducibility and enabling automation in RF analysis. Additionally, this advantage allows us to utilize temporary stations which measure only a few earthquakes.

Keywords Receiver functions · Autoencoders · Coherent · Deconvolution · Crustal Structure · Subduction

1 Introduction

Receiver functions (RFs), computed using several teleseismic earthquakes, provide a powerful method for investigating crustal and upper mantle structures below a particular receiver. This study focuses on analyzing the changes in the RF relative to the backazimuth and the distance to the teleseismic earthquake, which are essential for accurate subsurface characterization. Careful analysis of these variations and comparison with forward modeling results [Levin et al., 2008, Savage et al., 2007, Liu et al., 2015] can reveal important information about the orientation and magnitude of Earth's anisotropy, as well as the 3-D geometry of subsurface features, providing researchers with valuable insights into the

tectonic evolution and dynamics of a given region. To illustrate this emphasis, we consider the systematic variation of the PmS phase (forward-scattered S waves from the Moho caused by an incident P wave) with respect to backazimuth and distance. Numerous studies have extracted the fast-polarization direction and magnitude of crustal anisotropy from the PmS phase within RFs [McNamara and Owens, 1993, Bianchi et al., 2010, Zheng et al., 2018]. Similarly, backazimuth variations of the PmS phase in both radial and transverse RFs have been employed to calculate the dip azimuth, dip angle, and depth of subducting slabs [Shiomi and Park, 2008]. Zhu and Kanamori [2000] employed RFs generated by earthquakes that occur at various epicentral distances to determine the thickness of the crust and the P to S velocity ratio through semblance analysis.

To analyze RF variations with respect to backazimuth and earthquake distance, one must be able to compare RFs from multiple earthquakes. However, this task can be challenging due to the presence of pseudo-random *nuisance* effects. The nuisance effects are unique to each earthquake and it should be emphasized that the common assumption that these effects can be modeled as random Gaussian noise frequently proves inadequate [Kolb and Lekić, 2014]. To be precise, nuisance effects are unwanted signals in RFs that arise through two distinct pathways during the deconvolution of the radial with the vertical component of the seismogram. First, as deconvolution is ill-posed, it is susceptible to contamination by background seismic noise (owing to natural and human activities). This means that insufficient regularization in deconvolution amplifies the seismic noise linked to the spectral zeros of the source signature, which causes nuisance [Akuhara et al., 2019]. Conversely, when addressing the problem with regularization, nuisance appear as biases that are influenced by the choice of the regularization method. Secondly, deconvolution, which is associated with cross-correlation, results in crosstalk among non-converted P coda waves (arising from crustal heterogeneity) observed in the vertical and radial components [Park and Levin, 2000]. Crosstalk increases interference and makes interpreting converted seismic phases related to crustal structures (refer as crustal effects) more challenging. Various researchers [Park and Levin, 2000, Zhang et al., 2022, Zhang and Olugboji, 2024] have recognized that pseudo-random nuisance effects make it difficult to interpret receiver functions, highlighting the need to address these effects to achieve the accurate extraction of crustal characteristics. One strategy to improve the quality of RF involves the careful selection and identification of usable RFs through automated processes [Crotwell and Owens, 2005, Yang et al., 2016] and machine learning frameworks Gong et al. [2022], Krueger et al. [2021], Sabermahani and Frederiksen [2024]. However, this method overlooks the crustal signals present in noisy RFs, often completely disregarding them. Alternatively, another method focuses on reducing nuisance effects by denoising RFs. Due to the limited understanding of seismic sources, developing accurate models to represent nuisance effects is difficult, challenging the task of reducing or eliminating them. Moreover, these effects cannot be effectively removed through standard bandpass filtering techniques, as they share a frequency band similar to that of crustal converted phases. This paper seeks to separate and eliminate nuisance effects from RFs using an unsupervised deep learning framework, particularly focusing on symmetric autoencoders (SymAE).

In the literature, methods developed to minimize nuisance effects in RFs can be classified into two categories. The first category corresponds to data-driven methods. These methods average multiple RFs to improve the signal-to-noise ratio. Examples include

- stacking multiple earthquakes with a similar backazimuth and epicentral distance [Gurrola et al., 1995, Levin and Park, 1997, Hu et al., 2015, Bloch et al., 2023];
- weighted stacking techniques, such as the method proposed by Park and Levin [2000], that assess the level of incoherent nuisance in a RF within the frequency domain.

Stacking proves to be efficient when dealing with numerous RFs, especially when nuisance adhere to a simpler distribution like a Gaussian distribution. When analyzing the variations of RFs related to backazimuth or distance, these techniques can be limited by irregular earthquake distributions because certain azimuthal or epicentral distance bins might have more sources than others. This uneven distribution of earthquakes can potentially skew the stacked RFs, obscuring the actual crustal structure [Levin and Park, 1997, Ozakin and Ben-Zion, 2015, Bloch et al., 2023]. Weighted stacking techniques can be less robust due to the subjective nature of identifying high-quality RFs. The selection of weights can significantly influence the results and inconsistent or biased choices can introduce errors into the stacked RFs. Our approach is data-driven; nevertheless, unlike basic averaging methods, the encoder network within the SymAE framework is specifically trained to accumulate crustal influences across RFs from various earthquakes sharing similar backazimuth and epicentral distance parameters. This accumulation is similar to non-linear stacking technique [Schimmel and Paulssen, 1997], where the encoder network inherently evaluates the quality of each RF prior to stacking. To aid the encoder network in distinguishing between crustal effects and nuisance effects, we leverage the coherence of crustal effects across a collection of RFs obtained from proximal earthquakes. In a similar vein, Park and Levin [2000] introduced the concept of differentiating coherent crustal effects from incoherent nuisance in the frequency domain. We demonstrate that our deep learning approach overcomes the problem due to uneven earthquake-source spatial distribution as it needs fewer sources compared to linear stacking. The results of numerical tests show that

the accumulation of coherent crustal information from 20 distinct earthquake sources can effectively reduce nuisance effects.

Model-based techniques comprise the second category of methods aimed at minimizing nuisance effects. To improve RF quality, these methods rely on assumptions about Earth’s structure or nuisance effects characteristics. These methods, in particular, apply constraints to a gather of available RFs, ordered according to either backazimuth or epicentral distance. Examples include

- methods using sparsity-promoting random transforms [Olugboji et al., 2023], curvelet transforms [Chen et al., 2019], and singular spectrum analysis [Dokht et al., 2016] that assume a laterally homogeneous Earth model to filter linear events from the RF gather;
- supervised deep learning techniques [Wang et al., 2022] trained on assumed ensemble of crustal models, to directly determine crustal thickness and the P-to-S wave velocity ratio from the RFs;
- common conversion point (CCP) stacking [Zhu, 2000] of the RF gather, commonly used for imaging the Moho and mantle discontinuities, involves time-depth conversion based on a large-scale velocity model.

Several of the aforementioned model-based methods are unsuccessful when applied to intricate geological environments such as subduction zones, which are different from the assumed (simpler) models. These methods also require dense spatial coverage of earthquake events, which is challenging for temporary seismic stations. CCP stacking may result in artifacts [Zheng et al., 2014] due to mismatches between the velocity model and the Earth’s true model. An important drawback of supervised deep learning models is the difficulty in assessing their performance on real seismological data, which originates from a distribution that varies from that of the training data.

This paper presents an unsupervised framework, which operates without relying on labeled RF data for training. In unsupervised methods, networks autonomously extract features from the entire set of RFs, identifying underlying patterns without human input, thus proving effective for complex geological settings. For example, our network is trained on RFs from nearby earthquakes, irrespective of the signal-to-noise ratio of seismograms, to extract coherent features across the RFs. The focus of this unsupervised learning study is the use of autoencoders to derive meaningful representations of RFs. Autoencoders function by encoding each RF into a latent representation and subsequently decoding it back. Traditional autoencoders often produce complex latent representations of RFs, lacking clear physical interpretation and making it challenging to understand the captured features [Vincent et al., 2008, Chen et al., 2019, Dalai et al., 2021, M. Saad and Chen, 2020]. Several researchers [Ranzato et al., 2007, Makhzani et al., 2015, Bouchacourt et al., 2017, Mathieu et al., 2016] have suggested techniques for learning an interpretable latent representation using autoencoders. To address the interpretability issue, we used the symmetric autoencoder [Bharadwaj et al., 2022, SymAE], which disentangles *coherent features* in the grouped data within the latent space. Specifically, our approach assumes that crustal effects vary smoothly with epicentral distance or azimuth, unlike nuisance effects. This means that crustal effects remain coherent across a group of RFs derived from nearby earthquakes. SymAE enables us to integrate this assumption into auto-encoding, constraining, and identifying latent dimensions that correspond to crustal effects. Once SymAE was trained to learn a disentangled representation, Bharadwaj et al. [2022] demonstrated that coherent features could be transferred from one RF to another, thereby creating virtual RF. In this study, we assumed that nuisance effects are additive and proposed a method to produce virtual RFs with minimal nuisance effects. Ultimately, this approach offers a robust denoising technique with fewer assumptions regarding both the Earth model and nuisance statistics.

To validate our approach, we applied on synthetic RFs contaminated by non-Gaussian, unknown nuisance effects arising from measured earthquake source signatures and seismic noise. Two synthetic models were considered: an anisotropic layer model and a dipping layer model. In both instances, the MSE between the denoised RFs generated by SymAE and true nuisance-free RFs is consistently lower than that for RFs obtained through linear and phase-weighted stacking methods. We also applied our method on real data from seismic networks, including POLARIS, C8, CN, and UW, with the aim of imaging the Cascadia subducting slab beneath the southern Vancouver Island. Due to its multi-layered dipping slab and complex deformation processes [Nicholson et al., 2005, Audet et al., 2009, Bloch et al., 2023], the subduction zone is characterized by intricate scattering effects, resulting in unpredictable nuisance effects. This significantly hinders the extraction of reliable crustal effects from RFs in this region. Our radial RF results clearly display all the scattered S-waves generated by the three velocity interfaces of the subducting oceanic slab, as reported by Bloch et al. [2023]. Beyond radial receiver functions, our method effectively denoises transverse RFs, which often exhibit lower signal-to-noise ratios. More importantly, when applied to the Cascadia dataset, our method generates transverse RFs with quality superior to that of traditional stacking techniques. To validate the performance of our methodology, we conducted several checks. For example, our denoised RFs exhibited expected spatial consistency, with similar patterns observed at nearby seismic stations. Furthermore, our RFs calculated using nearby earthquakes demonstrated a high degree of agreement, confirming the robustness and reproducibility of our approach. Unlike many contemporary studies that exclude low signal-to-noise ratio (SNR) data, our method utilizes all available earthquakes,

expanding the azimuthal and epicentral distance coverage. This demonstrates the method’s resilience to noise and outliers. Finally, like any other deep learning method, our approach is computationally efficient, highly automated, and scalable to diverse datasets and geographical regions.

2 Training Receiver Function Data

Within the framework of an autoencoder, datapoints denote the input data used during training. In this research, each datapoint is equivalent to a set of RFs. The autoencoder is trained to map these datapoints into a compressed latent space and decode them to reconstruct the original input. This mechanism helps to discover efficient representations of the input data. This section outlines the procedure for computing RFs and organizing them into datapoints. The datapoints are formed with the specific aim of capturing coherent crustal information, thereby enhancing the autoencoder’s ability to meaningfully represent the input RFs.

2.1 Receiver Functions

The wavefield resulting from a teleseismic earthquake incident on the crustal structure of the Earth near a seismic station can be approximated as a planewave characterized by a seismic wavelet s and a propagation direction defined by the slowness vector \mathbf{p} . The interaction of this planewave with the crustal structure results in a measured waveform at the station, which can be expressed as a convolution of the seismic wavelet with the Earth’s impulse response:

$$\begin{aligned} d^z(t, \mathbf{p}) &= (s(t) * g^z(t, \mathbf{p})) + \epsilon^z(t) \\ d^r(t, \mathbf{p}) &= (s(t) * g^r(t, \mathbf{p})) + \epsilon^r(t). \end{aligned} \quad (1)$$

Here, temporal convolution is represented by $*$, and time is denoted as t . The vertical and radial components of the measured seismogram are indicated using d^z and d^r , respectively, while ϵ^z and ϵ^r represent uncorrelated noises in these components. The vertical and radial impulse responses of the crust beneath the seismic station, denoted g^z and g^r , are of particular interest in the imaging of the crust [Tauzin et al., 2019]. The seismic wavelet $s(t)$ contains information on the time function of the earthquake source and the propagation effects through the structure of the Earth from the source to the base of the crust. The generation of radial RF involves the deconvolution of the radial component with the vertical component to predominantly extract SV converted phases. As shown in Appendix A, the radial receiver function, after expressing the convolution operation in the time domain, is written as

$$r(t, \mathbf{p}) = \int_{\tau} s_a(t - \tau, \mathbf{p}) g^{r,z}(\tau, \mathbf{p}) d\tau + \epsilon(t, \mathbf{p}), \quad (2)$$

where s_a denotes a zero-phase signal convolved with $g^{r,z}$, which depicts the cross-correlation between g^r and g^z . We used ϵ to denote the nuisance effects arising from the cross-correlation between seismic noise (ϵ^r and ϵ^z) and the crustal impulse responses (g^z and g^r). The purpose in the subsequent sections is to extract $g^{r,z}$, building on the aforementioned decomposition of the RF, which can also be easily expanded to demonstrate the case for transverse displacement components.

2.2 Single Station: RF Grouping

Changes in r as a function of \mathbf{p} can result from the geometry and anisotropy of the crust (specified by $g^{r,z}$) or from nuisance terms (specified by s_a and ϵ). To isolate variations due to crust, we assume that the factor $g^{r,z}$ changes smoothly with the slowness vector \mathbf{p} , in contrast to the terms s_a and ϵ , which fluctuate rapidly since each \mathbf{p} corresponds to a distinct earthquake with a unique source time function. Essentially, when analyzing the RFs of teleseismic earthquakes situated closely together, the crustal effects are *coherent*. This assumption is vital in grouping RFs to produce datapoints for training SymAE, allowing the SymAE network to differentiate between crustal effects and nuisance effects in the RFs.

In pursuit of creating datapoints for SymAE, we sorted the RFs into groups by initially establishing bins based on chosen intervals of backazimuth and epicentral distance. The smaller the intervals, the fewer RFs each group contains. We selected the intervals to ensure that each group has no fewer than approximately 10 RFs, which is optimal to effectively apply SymAE. In practical scenarios, the function r as described in Eq. 2 can be computed for particular discrete time points and slowness vectors. Group assignment involves associating each unique slowness vector value with a specific bin, determined by the corresponding backazimuth and epicentral distance ranges. In our convention, subscripts signify the particular bin associated with the RF. The superscripts denote the index corresponding to the specific earthquake whose seismograms are used to compute the RF. Additionally, vectors after time discretization are

denoted by boldface symbols. According to this notation, the RF derived from the seismograms of the i -th earthquake located in the j -th bin, after discretization, is expressed as

$$\mathbf{r}_j^{(i)}[t] = \sum_{\tau} \mathbf{s}_a^{(i)}[t - \tau] \mathbf{g}_j^{r,z}[\tau] + \boldsymbol{\epsilon}^{(i)}[t], \quad i = 1, 2, 3, \dots, n_j, \quad (3)$$

We utilized square brackets, such as $[t]$, to index vectors, marking specific time samples. Here, $\mathbf{r}_j^{(i)} \in \mathbb{R}^{n_t}$, where n_t represents the number of time samples. We adjusted the P-wave amplitude at $t = 0$ to 1 across all RFs. The notation n_j signifies the count of RFs within the j -th bin. It is crucial to highlight that the assumption of coherent crustal effects suggests that $\mathbf{g}^{r,z}$ is independent of the earthquake index i within the group.

2.3 Numerical Simulation of Coherent Crustal Effects

At crust-mantle boundary, an incoming plane P wave produces S waves through conversion (PS). Moreover, the converted phases could be reflected by the free surface, such as PsS, or when a P-wave is reflected off the free surface, it might transform into S waves, like PpS. Fig. 1 illustrates some of these crustal phases that compose crustal impulse responses g^z and g^r . To demonstrate the coherence of crustal phases in RFs within a bin, it is necessary to illustrate that both their kinematics and amplitudes vary smoothly with changes in backazimuth and epicentral distance. Toward this end, synthetic RFs were produced with the help of the PyRaysum package [Bloch and Audet, 2023], simulating Earth’s crust atop a high-velocity mantle half-space. To examine how crustal phases change with backazimuth, we first use a crustal model featuring an anisotropic layer with 7% transverse anisotropy and a 10° dip from the horizontal. The radial RFs for this model are plotted in Fig. 1a, which illustrate the changes (due to anisotropy) in the arrival times and amplitudes of crustal phases across different backazimuths. It is crucial to note that RFs exhibit coherence within a narrow range of backazimuths. Additionally, in the figure, a rectangle highlights the backazimuth bin with a size 10° used in the synthetic experiment (detailed in Sec. 4). Similarly, we now analyze how changes in epicentral distance affect the outcomes. The crustal model shown in Fig. 1b features a layer inclined at 15° from the horizontal and oriented along N30°W. This results in changes in the crustal phases PS and PpS as the epicentral distance varies, reflecting the geometric configuration of the crust. Note that when examining a narrow range of epicentral distances (e.g. in an epicentral bin marked using a rectangle), the RFs remain coherent. In conclusion, these simulations illustrate that within a backazimuth epicentral-distance bin, the impact of the crust on the RFs shows minimal variation, confirming our assumption.

2.4 Multiple Stations and Datapoints for Training

A training datapoint for SymAE is represented as a vector

$$\mathbf{r}_j = [\mathbf{r}_j^{(1)}, \mathbf{r}_j^{(2)}, \dots, \mathbf{r}_j^{(n_j)}]. \quad (4)$$

Each datapoint collects all the RFs associated with a specific bin, specifically the j -th bin, which is characterized by backazimuth and epicentral distance. The total number of training datapoints corresponds to the number of available bins. For an individual receiver, this number is influenced by the number of earthquakes it records and their geographical distribution. In our research, we train using datapoints from multiple stations simultaneously. Thus, the total number of datapoints is the aggregate of all bins across these receivers. Our main objective is to detect variations in coherent crustal information between different datapoints, despite the presence of varying nuisance effects. The training dataset is the collection of all datapoints

$$\mathbf{X} = \{\mathbf{r}_j \mid 1 \leq j \leq N_b\}, \quad (5)$$

where N_b indicates the total quantity of bins from various stations.

In conclusion, while this section is focused on radial RFs, datapoints can also be constructed for transverse RFs. Moreover, this approach to the construction of datapoints can be extended to RFs resulting from different seismic phases, such as S, SKS, and PKP. The application of our methodology to these additional phases is reserved for future study.

3 Symmetric Autoencoders

In this part, we focus on the task of learning representations of RFs using a symmetric autoencoder [Bharadwaj et al., 2022, SymAE]. Representation learning can be conceptualized as a method that encompasses both forward and inverse problems.

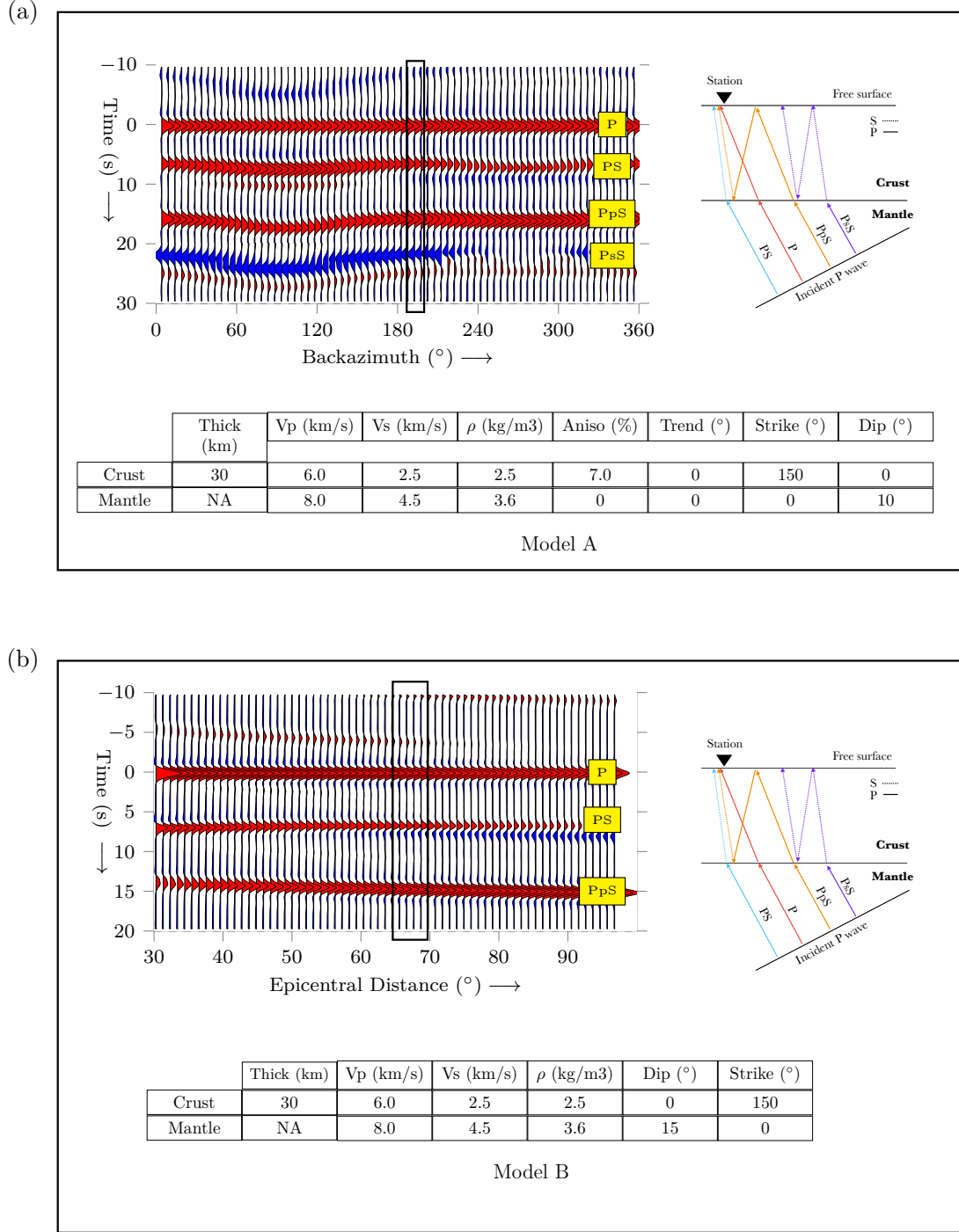


Figure 1: Synthetic radial receiver functions demonstrating the smooth variation with (a) backazimuth and (b) epicentral distance (b). The two models considered were: (a) one incorporating anisotropy, which allows for variation in receiver functions with backazimuth, and (b) one assuming an isotropic Earth structure. The seismic phases of interest, generated at the Moho, are marked. This figure illustrates the assumption of coherent crustal effects within bins defined by the backazimuth and epicentral distance. The rectangular boxes indicate the bin widths used in this study. On the left, the raypaths of seismic waves produced at the Moho by an incoming P-wave are shown.

- Inverse problem (inference to obtain a latent code): The process of extracting meaningful features or representations from the input RF data can be seen to solve an inverse problem. In this scenario, for a datapoint \mathbf{r}_j ,

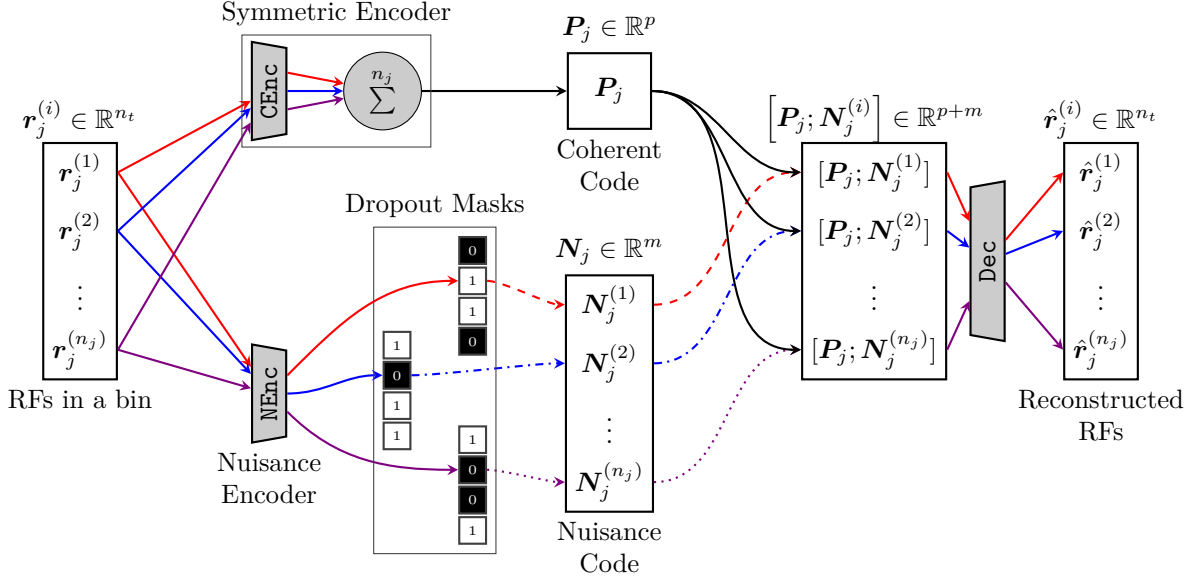


Figure 2: Schematic illustration of symmetric autoencoders network. The network takes as input a set of RFs from a single azimuth-epicentral-distance bin. Separate encoder networks, namely the symmetric encoder and the nuisance encoder, encode the coherent crustal effects and incoherent nuisance effects of the RFs, respectively. Dropout masks are applied to prevent propagation of coherent information. The coherent and nuisance latent codes from the two encoder networks are then fused, and the resulting representation is decoded to reconstruct the original RFs. Solid arrows show the propagation of coherent information. This architecture allows the network to learn disentangled representations of the coherent crustal effects and incoherent nuisance effects, enabling the removal of the nuisance effects.

the objective is to identify a latent code \mathbf{H}_j that captures both the crustal effects and the nuisance effects that contribute to the formation of \mathbf{r}_j . This step is achieved through an encoder network Enc to produce the code

$$\mathbf{H}_j = \text{Enc}(\mathbf{r}_j), \quad (6)$$

where the encoder maps the input data to a latent space. Solving this inverse problem is crucial because it transforms the RFs into a compact, informative representation that facilitates further processing.

- Forward problem (reconstruction of RFs): The second phase involves solving a forward problem, where the task is to reconstruct the original RFs from the latent code \mathbf{H}_j . This step is performed using a decoder network Dec, which generates the output RFs

$$\hat{\mathbf{r}}_j = \text{Dec}(\mathbf{H}_j). \quad (7)$$

The decoder aims to transform the latent code back into a space similar to the original data.

The encoder and decoder networks are optimized by reducing the reconstruction loss

$$J = \sum_j \sum_i \|\mathbf{r}_j[i] - \hat{\mathbf{r}}_j[i]\|_2^2, \quad \text{where } \hat{\mathbf{r}}_j = \text{Dec}(\text{Enc}(\mathbf{r}_j)). \quad (8)$$

Here, $\|\cdot\|_2$ denotes the Euclidean norm. Reducing J leads the model to develop an effective latent representation. Essentially, the encoder compresses the information efficiently, while the decoder evaluates how well and accurately the latent representation reflects the original data. In training, the goal of achieving a reconstruction with a reduced J suggests that \mathbf{H}_j probably preserves the crucial features of \mathbf{r}_j .

Unlike traditional autoencoders [Hinton and Salakhutdinov, 2006, Ng, 2011, Vincent et al., 2008], the SymAE encoder network is uniquely designed to solve two distinct inverse problems, producing two separate latent codes. The architecture of SymAE is highlighted in Fig. 2. The first inverse problem involves estimating the crustal effects shared among the RFs of \mathbf{r}_j , while the second focuses on estimating the nuisance effects specific to each RF element within \mathbf{r}_j . The entire latent code \mathbf{H}_j is constructed by combining the results from these two separate inverse problems. Upon estimating the crustal and nuisance effects for each datapoint, during the decoding stage (forward modeling), we can opt

to apply these effects across various datapoints — this capability allows us to create virtual RFs that were not originally recorded. In essence, the dual-inverse problem approach facilitates forward modeling by allowing nuisance effects to be transferred from one RF to another. In summary, our results indicate that once the training of the encoder and decoder networks within SymAE is complete, they can generate virtual RFs with a better signal-to-noise ratio. This improvement enhances the crustal effects while minimizing the influence of nuisance effects. Before delving into this topic, let us first explore the architectural aspects of SymAE.

SymAE consists of two distinct encoders: a symmetric encoder (PEnc) and a nuisance encoder (NEnc), which transform the RFs in \mathbf{r}_j into coherent and nuisance latent codes, respectively. The details of these encoders are described below.

3.1 Symmetric Encoder

The PEnc is a deep neural network designed to identify coherence or similarity among RFs within \mathbf{r}_j . Essentially, the architecture of PEnc ensures that, when applied to \mathbf{r}_j , it generates a latent code $\mathbf{P}_j \in \mathbb{R}^p$ that represents only coherent crustal effects, excluding nuisance effects. According to the universal approximation theorem Hornik et al. [1989], Cybenko [1989], an unconstrained PEnc would capture both coherent crustal effects and nuisance effects. Consequently, PEnc is subject to a permutation invariance constraint, ensuring that the order of the RFs in \mathbf{r}_j does not affect the output of the network PEnc. Mathematically, this means that

$$\mathbf{P}_j = \text{PEnc}(\mathbf{r}_j) = \text{PEnc}(\Pi(\mathbf{r}_j)). \quad (9)$$

Here, Π is a random permutation function that reorders the elements of \mathbf{r}_j according to a random permutation Π of the indices $\{1, 2, \dots, n_j\}$, i.e.,

$$\Pi(\mathbf{r}_j) = [\mathbf{r}_j[\Pi(1)], \mathbf{r}_j[\Pi(2)], \dots, \mathbf{r}_j[\Pi(n)]] , \quad (10)$$

where Π is a bijection $\Pi : \{1, 2, \dots, n\} \rightarrow \{1, 2, \dots, n\}$ that shuffles the indices of \mathbf{r}_j randomly. The central concept is to consider PEnc as addressing the inverse problem of inferring crustal effects from RFs derived from various nearby earthquakes. The solution to this inverse problem remains unchanged regardless of the sequence in which the earthquakes are recorded by the station, illustrating permutation invariance. In essence, maintaining the permutation invariance in PEnc promotes the inference of crustal effects. Alternatively, by imposing permutation invariance, we ensure that nuisance effects, which differ among RFs, cannot be accurately inferred by PEnc. The above constraint implies that the function $\text{PEnc}(\mathbf{r}_j)$ maintains symmetry in terms of the sequence of RFs within \mathbf{r}_j , thus we refer to it as a symmetric encoder.

In practice, we adopt the network architectures outlined in Zaheer et al. [2017] that can approximate functions with permutation-invariance properties. Specifically, we employ the mean operation over RFs as the permutation-invariance mechanism after applying a neural network CEnc on each element of $\Pi(\mathbf{r}_j)$, resulting in the coherent code as follows:

$$\mathbf{P}_j = \text{PEnc}(\mathbf{r}_j) = \sum_{i=1}^{n_j} (\text{CEnc}(\mathbf{r}_j[i])). \quad (11)$$

The mean operation maintains symmetry with regard to the sequence of RFs, thus ensuring the required permutation invariance for PEnc, as described in Eq. 9. This architectural constraint applied to PEnc is demonstrated in Fig. 2. In this figure, solid arrows represent the propagation of coherent crustal information across the SymAE network.

3.2 Nuisance Encoder

SymAE is designed to reconstruct the input datapoint without loss of information, requiring its encoder to infer both the coherent crustal effects and the nuisance effects. Since the coherent encoder cannot infer nuisance effects, SymAE uses another encoder, called the nuisance encoder NEnc, to estimate these effects. Two features define NEnc : 1) it lacks the architectural constraints (i.e. symmetry) found in PEnc, being instead constrained during training through stochastic regularization [Wang and Manning, 2013, Kingma et al., 2015]; 2) the network operates on each element of the datapoint \mathbf{r}_j , similar to performing independent inferences on each RF to estimate the respective nuisance effects. The nuisance influences within each RF are represented by the code $\mathbf{N}_j^{(i)} \in \mathbb{R}^m$, defined as follows:

$$\mathbf{N}_j^{(i)} = \mathfrak{N}(\text{NEnc}(\mathbf{r}_j[i])). \quad (12)$$

In this context, the function \mathfrak{N} introduces random perturbations to $\mathbf{r}[i]$ throughout the training process, serving as a form of stochastic regularization. This can be interpreted as introducing noise to the estimates of NEnc. Essentially, we are indicating to the decoder that the inference of NEnc carries some uncertainty, thereby compelling the decoder to place greater reliance on the estimates from the symmetric encoder.

In practice, \mathfrak{N} is implemented using Bernoulli dropout [Srivastava et al., 2014], as illustrated in Fig. 2, throughout training to introduce high probability random perturbations into the nuisance code. It is important to observe that, unlike the traditional use of dropouts for regularizing functions approximated by deep neural networks, SymAE employs dropouts to avoid the nuisance encoder unintentionally capturing coherent crustal effects.

3.3 Decoder

The encoders are responsible for inferring both crustal and nuisance effects, generating latent codes denoted \mathbf{P}_j and $\mathbf{N}_j^{(i)}$. The decoder is tasked with utilizing these latent codes to perform forward modeling, thereby reconstructing the RFs within each datapoint. To achieve this, the decoder network is trained to create each element of the output datapoint $\hat{\mathbf{r}}_j$. This network takes as input a concatenated latent code, formed from latent codes produced by both symmetric and nuisance encoders. For the i -th element of the j -th datapoint, we represent the concatenated latent code as

$$\mathbf{H}_j^{(i)} = [\mathbf{P}_j; \mathbf{N}_j^{(i)}]. \quad (13)$$

Subsequently, this concatenated latent code is inputted to a deep neural network Dec, facilitating the generation of a RF:

$$\hat{\mathbf{r}}_j^{(i)} = \text{Dec}(\mathbf{H}_j^{(i)}) \quad (14)$$

This is demonstrated in Fig. 2. Finally, output datapoint is formed as a vector of all the generated RFs

$$\hat{\mathbf{r}}_j = [\hat{\mathbf{r}}_j^{(1)}, \hat{\mathbf{r}}_j^{(2)}, \dots, \hat{\mathbf{r}}_j^{(n_j)}]. \quad (15)$$

In summary, SymAE effectively reconstructs the data without much loss utilizing two types of encoder: coherent and nuisance encoders. These encoders have their individual strengths and weaknesses, but work together in a complementary manner to accurately reconstruct the original RFs. The model involves three neural networks, denoted PEnc, NEnc, and Dec, which are trained simultaneously to minimize the reconstruction loss specified in Eq. 8. We used neural networks similar to Alex-net [Krizhevsky et al., 2012], integrating convolutional, pooling, and fully connected layers to define encoders. In selecting the hyperparameters for SymAE, such as the latent code length, the dropout rate during training, and additional parameters related to the convolutional layers in both the encoder and decoder, we conducted synthetic experiments. The following sections elaborate on the use of these functions after training.

3.4 Generating Virtual RFs

Consider a trained SymAE model. Coherent codes can be produced for each datapoint, while nuisance codes can be produced for each specific RF. These latent codes lack direct interpretability. One of the most intriguing uses of SymAE highlighted in Bharadwaj et al. [2022] is the generation of virtual seismograms. This process entails decoding a hybrid or custom latent code. The synthesized virtual RFs are not present in the original training dataset; instead, they perform interpolation amongst the RFs within the training dataset. For example, consider two RFs, $\mathbf{r}_j^{(1)}$ and $\mathbf{r}_k^{(2)}$, with their respective latent codes $[\mathbf{P}_j; \mathbf{N}_j^{(1)}]$ and $[\mathbf{P}_k; \mathbf{N}_k^{(2)}]$ produced by the encoder. By decoding a custom latent code, such as $[\mathbf{P}_j; \mathbf{N}_k^{(2)}]$, a virtual RF can be generated:

$$\mathbf{v}_{j,k}^{(2)} = \text{Dec}([\mathbf{P}_j; \mathbf{N}_k^{(2)}]). \quad (16)$$

Similarly,

$$\mathbf{v}_{k,j}^{(1)} = \text{Dec}([\mathbf{P}_k; \mathbf{N}_j^{(1)}]).$$

Fig. 3 gives a visual illustration of the process of generating virtual RFs for $j = 3$ and $k = 1063$. In this case, RFs from the synthetic dataset — explained in detail later — are utilized. From the figure, we can observe that the nuisance effects of an actual RF Fig. 3(c) is inherited by the virtual RF Fig. 3(d). On the other hand, virtual RF $\mathbf{v}_{j,k}^{(2)}$ maintains the same crustal effects as $\mathbf{r}_j^{(1)}$ while incorporating the nuisance effects of $\mathbf{r}_k^{(2)}$. It should be noted that nuisance code is necessary to synthesize virtual RFs, as coherent code alone is insufficient. Virtual RFs can be systematically generated for each bin by iterating through all available bins to create a comprehensive set:

$$\mathbf{V}_k^{(2)} = \{\mathbf{v}_{j,k}^{(2)} \mid 1 \leq j \leq N_b\}. \quad (17)$$

Since every element within this set is affected by identical nuisance effects, we are now closer to our goal of comparing crustal effects across different epicentral-azimuthal bins. However, despite having aligned the nuisance effects for all

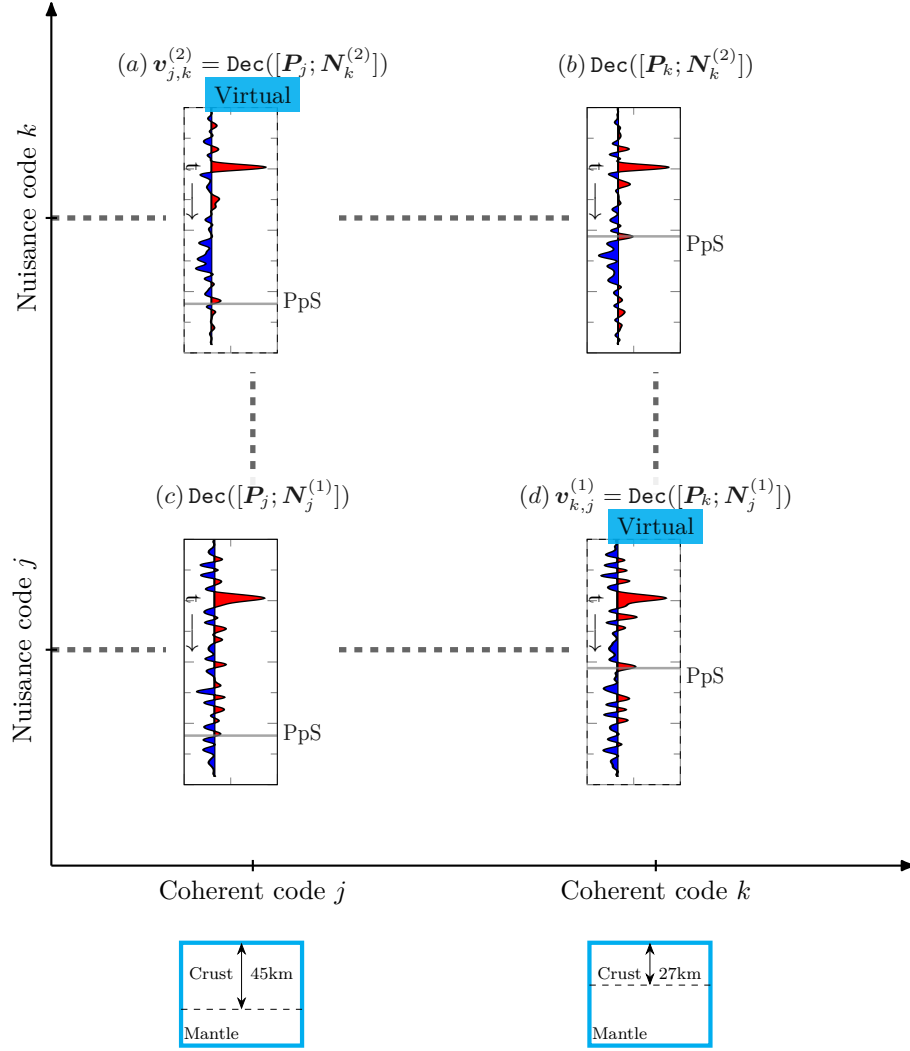


Figure 3: This figure illustrates the swapping of coherent and nuisance latent codes to generate virtual RFs. The coherent code captures crustal effects, while the nuisance code captures nuisance effects. In this figure, (b) and (c) illustrate reconstructed radial RFs. Virtual radial RFs shown in (a) and (d) are formed by decoding hybrid swapping the nuisance code \mathbf{N} and the coherent code \mathbf{P} respectively. The pairs (a, b) and (c, d) are observed to have the same nuisance effects but differ in crustal effects, as demonstrated by the kinematics of PpS, which is marked using a black horizontal line.

	Thickness (km)	Vp (km/s)	Vs (km/s)	ρ (kg/m ³)	Aniso. (%)	Trend (°)	Strike (°)	Dip (°)
Layer 1	27.0	6.0	3.45	2.8	10.0	0	0	0
Layer 2	NA	8.04	4.47	3.6	0	0	0	0

Table 1: Parameters of Model 1. This model includes a flat anisotropic layer with 10% transverse anisotropy, with the fast-axis oriented at 0°N.

	Thickness (km)	Vp (km/s)	Vs (km/s)	ρ (kg/m ³)	Aniso. (%)	Trend (°)	Strike (°)	Dip (°)
Layer 1	27.0	6.0	3.55	2.8	10.0	0	0	0
Layer 2	5.0	5.4	2.8	2.5	0	0	0	20
Layer 3	12.0	6.29	3.7	3.0	0	0	0	20
Layer 4	NA	8.04	4.47	3.6	0	0	0	20

Table 2: Parameters of Model 2. This model incorporates an anisotropic layer (10% transverse anisotropy) overlaying two dipping layers (10° dip). It depicts seismic stations over subducted oceanic plates.

elements in $\mathbf{V}_k^{(2)}$, we have yet to achieve denoising, as RFs are still commonly affected by the nuisance effects of $\mathbf{r}_k^{(2)}$. To effectively remove common nuisance effects within a set of RFs, we employ the technique of *mean-subtraction*. This process helps clarify the interpretation of virtual RFs by highlighting differences in crustal effects while reducing the impact of nuisance effects. Consider a collection of RFs denoted as $\{\mathbf{r}_j^{(i)} \mid 1 \leq i \leq n_j\}$. A revised set of RFs is created by individually adjusting each RF, subtracting the average of the entire set through the expression:

$$\{\mathbf{r}_j^{(i)} - \frac{1}{n_j} \sum_{i=1}^{n_j} \mathbf{r}_j^{(i)} \mid 1 \leq i \leq n_j\}. \quad (18)$$

When the same additive nuisance effects impact all RFs within the set, the mean-subtraction method efficiently removes them. Appendix B provides a further justification for mean-subtraction and its application to eliminate additive nuisance effects.

4 Synthetic Experiments

In this section, we evaluated our method by creating synthetic receiver functions with realistic nuisance using two distinct crustal velocity models. In particular, we assessed SymAE’s performance by calculating the mean-squared error between true synthetic RFs devoid of nuisance and the virtual RFs. Our methodology for generating synthetic RFs involves a multistep process described below. Synthetic experiments helped us adjust the network hyperparameters before applying SymAE to real data. Our results, compared to linear and phase-weighted stacking, show that SymAE outperforms both techniques.

4.1 Synthetic Crustal Models

Two velocity models were employed for the synthetic experiment. 1. Model 1, as detailed in Tab. 1, includes a single layer exhibiting transverse anisotropy. This model is characterized by a crust with 10% anisotropy, positioned above an isotropic mantle. The anisotropic layer has the fast axis oriented at an azimuth angle of 0°N. 2. Model 2 consists of three isotropic layers with dips as detailed in Tab. 2. The layers dipped 20° from the horizontal with a strike of 0°N. This model represents a subduction zone that features two dipping layers beneath a crust that exhibits transverse anisotropy. Six stations (Stations 1–6) were considered in both models, with the thickness of the first layer progressively increasing from Station 1 to Station 6. Anisotropy in both models leads to systematic variations in PS-wave propagation along the backazimuth, whereas the interface dip leads to variations with epicentral distance. Following the RF calculation, we demonstrate how the presence of nuisance effects complicates the interpretation of layer geometry and anisotropy when attempting to extract the aforementioned variations.

4.2 Data Preparation

The detailed steps to generate synthetic RFs for the models described above are as follows.

- Crustal impulse response calculation. At each station, the crustal impulse responses for the vertical (Z), radial (R), and transverse (T) components were calculated using the PyRaysum software [Bloch and Audet, 2023]. The backazimuth and epicentral distance were binned with a 10° interval. At each bin, crustal impulse responses were generated for randomly selected backazimuth and epicentral distance within the bin’s range. The count of impulse responses assigned to each bin was randomly set, varying between 15 and 30. This simulates the scenario where certain bins experience more earthquakes than others.
- Convolution with real seismograms. Each crustal impulse response was convolved with a distinct real seismogram, trimmed 20 s before and after the P-wave arrival, to create synthetic seismograms. This method replicates the variations in bandwidth and zeros seen in the source spectrum commonly observed in actual earthquakes. Each real seismogram was uniquely selected without replacement from a large dataset, and the resulting synthetic seismograms were bandpass filtered between 0.005 and 1 Hz.
- Noise addition. Random Gaussian noise, bandpass filtered within the same frequency range as the synthetic seismograms, was added to all three components independently. The noise level was adjusted to maintain a specified signal-to-noise ratio (SNR), which was randomly selected from a log-normal distribution. The SNR was determined by comparing the root-mean-square (rms) amplitude in a 10 s interval after the arrival of the P wave to the rms amplitude in a 10 s interval before the arrival of the P wave, both measured on the vertical component of the seismogram.
- Generation of receiver functions. Frequency domain deconvolution was employed to generate synthetic radial and transverse receiver functions. The additive noise in the seismograms was capped at a maximum SNR of 2. The deconvolution process was regularized using a water level parameter of 0.01 and a Gaussian filter with a width of 5. The resulting receiver functions (RFs) were normalized with respect to the P wave at $t = 0$.
- Datapoints and binning. We created datapoints by dividing the 0° – 360° backazimuth into 10° intervals and dividing the 40° – 100° epicentral distance also into 10° intervals. This procedure results in $36 \times 6 \times 6$ datapoints per model, corresponding to the number of azimuth bins, epicentral distance bins, and receivers.

In addition to the RFs with nuisance effects described above, true radial and transverse RFs were created using the same procedure. This involved using a Gaussian pulse as the source wavelet and excluding any additive noise. These true RFs are crucial for assessing performance, although they are not needed for training.

4.3 Virtual RFs

For both synthetic Earth models, each datapoint was divided so that 80% of the RFs were used for training, while the remaining 20% were reserved for testing. The datapoints for each of the Earth models were processed after two separate SymAE models were initialized independently. In addition, datapoints for the radial and transverse components were trained independently. The number of convolutional layers in the encoders was determined on the basis of the learning curve, ensuring an optimal balance between model complexity and overfitting. The coherent code length (p) and the nuisance code length (m) were fixed at 200 and 80 respectively. Early stopping was implemented with a maximum of 30 epochs and a learning rate of 0.0004 was employed. The optimal dropout rate at the output of the nuisance encoder was fixed to 0.3. After training the network on the datasets, we computed a virtual RF without nuisance effects for each datapoint at all stations, as described in Sec. 3.4. To generate RFs with identical nuisance effects, we use the nuisance code from an RF with minimal nuisance effects, typically one with a high SNR. Our experimental findings indicate that the selection of this nuisance code, provided that it is derived from a high-SNR RF, led to consistent results. The mean-subtraction operation (Eq. 18) assumes that the mean of the crustal effects across all data points is negligible (see Appendix B). This is ensured by selecting a varied array of receiver stations in the synthetic model, where we gradually increase the thickness of the initial layer from Station 1 to Station 6.

We begin by examining the results of Model 1. The anisotropy resulted in variations in the arrival times of the crustal phases based on the backazimuth. Fig. 4 shows the virtual, stacked, and true RFs (after mean-subtraction) for Station 1, plotted against backazimuth. Here, for plotting, all the RFs are chosen from an epicentral bin 40° – 50° . We stacked RFs within the bins using two methods: linear stacking and phase-weighted stacking (PWS) with $\nu = 0.8$ [Schimmel and Paulssen, 1997]. The virtual RFs, after mean-subtraction, are cleaner and more closely resemble the true RFs compared to the stacked RFs; i.e., most of the crustal phases present in the true RFs are reproduced in the virtual RFs, unlike stacked RFs. It can also be noticed that the transverse virtual RFs are also enhanced compared to stacking. The comparisons of mean squared error (MSE) between individual RFs and their true counterparts (Fig. 5) consistently show lower values for virtual RFs compared to stacked RFs, highlighting a better match to the true RFs. The virtual RFs exhibit improved SNR compared to stacked RFs at other stations as well — the detailed results can be found in the supplementary material. Notably, we observe an increase in the MSE as the depth of the initial crustal interface grows; for instance, surface multiples beyond 10 s are not effectively obtained at Stations 4, 5, and 6. This is due to the increase

in depth of the crustal interface, which results in greater variability of the converted phases within a bin, thereby causing a loss of coherency. We proceed with examining the outcomes derived from Model 2, which added complexity with dipping layers, focusing once more on the variations in arrival times and amplitudes as a function of backazimuth. Fig. 6 illustrates the virtual, stacked and actual RFs for Station 1. Similar to the case of Model 1, the virtual RFs consistently showed a lower MSE (Fig. 7) than the two stacking techniques. Notably, there is an improved resolution of closely situated crustal phases in the radial component. Additionally, the polarity reversal of seismic phases in the transverse component is accurately represented in the virtual RFs, unlike in stacked RFs. The findings validate the use of SymAE for the analysis of RFs in intricate geological environments. The supplementary material includes results for all other stations.

5 Cascadia Subduction Zone

RF studies have been widely utilized to characterize crustal structures in subduction zones [Cassidy, 1995, Bloch et al., 2023, Savage et al., 2007, Shiomi and Park, 2008]. However, the complex structural settings in the subduction zones of ocean plates, which include low-velocity zones, partial melting, and accretionary prisms, due to geodynamic processes, present significant obstacles in the extraction of crustal structures from RFs. The complex scattering of different seismic phases poses significant challenges for interpreting RFs, primarily due to the presence of nuisance effects. Conventional methods for the removal of nuisance effects, such as stacking and supervised denoising, are inefficient for complex crustal structures in subduction zones. The Cascadia Subduction Zone, in particular, has been the focus of extensive study due to its intricate slab morphology, link to seismic hazards, and geodynamic processes [Langston, 1979, Nicholson et al., 2005, Bloch et al., 2023]. Bloch et al. [2023] and Audet et al. [2009] characterized the subducting oceanic slab as a system of two dipping layers: a low-velocity zone overlaying a higher-velocity zone, using receiver functions. To reduce nuisance effects, Bloch et al. [2023] and Audet et al. [2009] filtered noisy seismograms based on the signal-to-noise ratio and linearly stacked RFs within the bin. In this section, we reexamine the data and demonstrate that SymAE improves the extraction of converted phases from both radial and transverse RFs. In particular, we do not filter out noisy seismograms and fully automate the procedure, utilizing all available RFs. The reason behind this is that even seismograms with low SNR, which originate from earthquakes of lower magnitudes, can still yield important information.

5.1 Data Preparation

We used teleseismic earthquake data from 42 seismic stations located in southern Vancouver Island, British Columbia, and the Olympic Peninsula, belonging to the POLARIS [Geological Survey of Canada, 2000], C8 [Geological Survey of Canada, 2002], CN [Natural Resources Canada, 1975] and UW [University of Washington, 1963] networks (Fig. 8). Earthquakes with epicentral distances ranging from 30° to 100° and a minimum moment magnitude of 5.5 were used. The seismograms were rotated to radial and transverse components, then bandpass filtered from 0.03 to 3.0 Hz, and cut to begin 20 s preceding the PREM-calculated P wave and end 50 s following it. Radial and transverse RFs were generated for all available seismograms, regardless of the SNR, using water-level deconvolution code from the Seispy package [Xu and He, 2022] with a Gaussian factor of 5.0 and a water level of 0.01. These RFs were binned according to the backazimuth using bin sizes of 8° and epicentral distance using bin sizes of 5° . Excluding bins with fewer than 2 RFs resulted in 2491 datapoints across 42 stations. In each datapoint, 80% of the RFs were allocated for training and 20% for testing. We used the same architecture as in the synthetic experiment, but the coherent code length and nuisance code length were fixed at 70 and 300, respectively. The optimal dropout rate at the output of the nuisance code was fixed at 0.3. We also applied early stopping of the training process at 30 epochs to avoid overfitting. To interpret and visualize the dip of the subduction slab, we have chosen 18 stations located along a transect in southern Vancouver Island, as shown in Fig. 8.

Phase	Notation
Forward scattered S wave from top velocity contrast	P_tS
Backward scattered S wave from middle velocity contrast	Pp_cS
Backward scattered S wave from bottom velocity contrast	Pp_mS

Table 3: This table illustrates the phases and their respective symbols as referenced in Bloch et al. [2023]. According to Bloch et al. [2023], the subducting slab beneath the southern Vancouver Island is conceptualized with two distinct layers: one being a low-velocity layer resting above the oceanic crust. This configuration causes a negative velocity contrast at the top interface and two positive velocity contrasts: one occurs between the low-velocity layer and the oceanic crust, and the other occurs between the oceanic crust and the mantle.

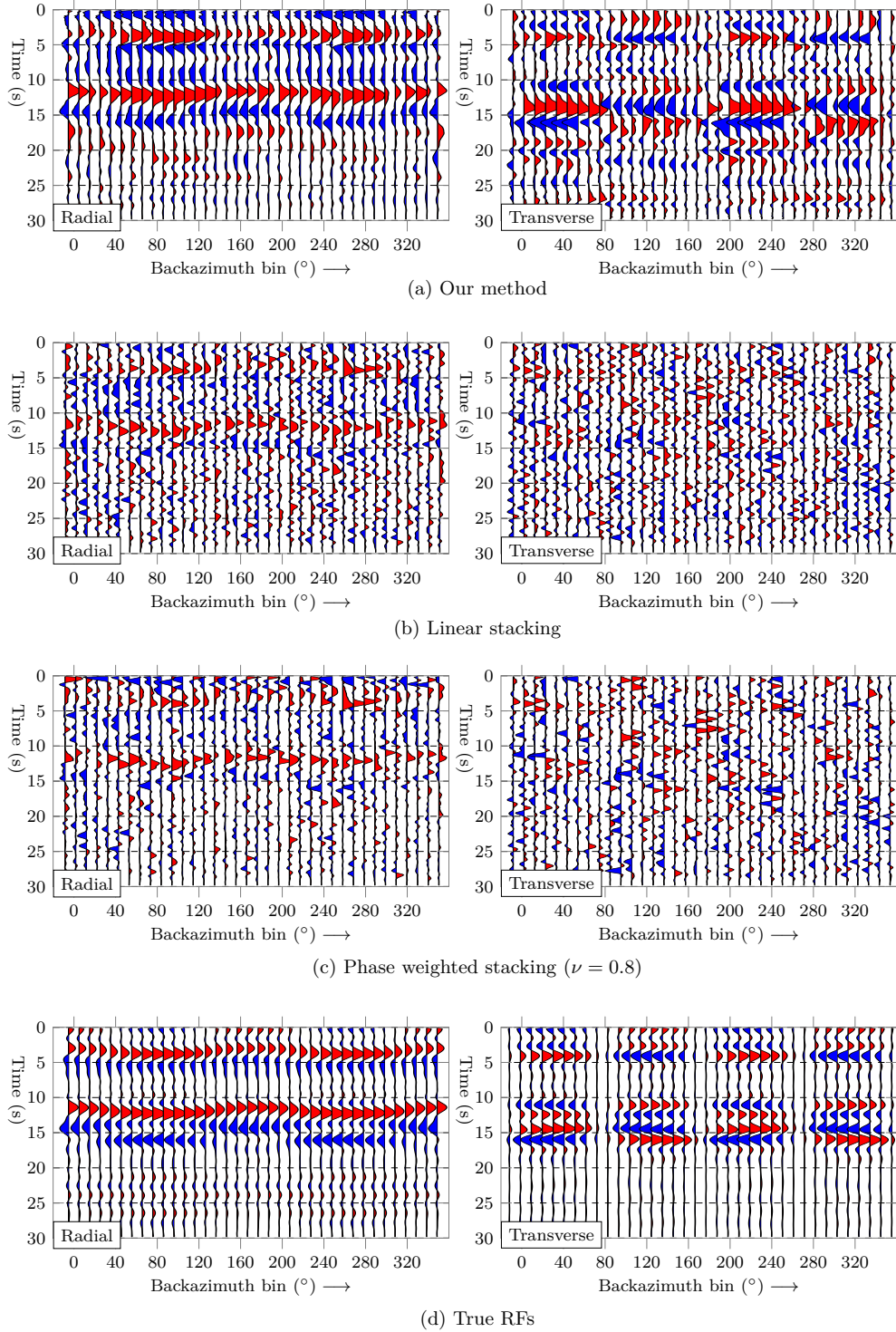


Figure 4: This figure shows radial and transverse RFs from all backazimuth bins for Station 1 (Model 1). a) Virtual RFs from the proposed method. b) RFs after bin-wise linear stacking. c) RFs after bin-wise phase-weighted stacking (PWS). Virtual RFs resemble the true RF more closely than the stacked RFs. Note that no P phase at $t = 0$ is observed in all RFs due to the mean-subtraction.

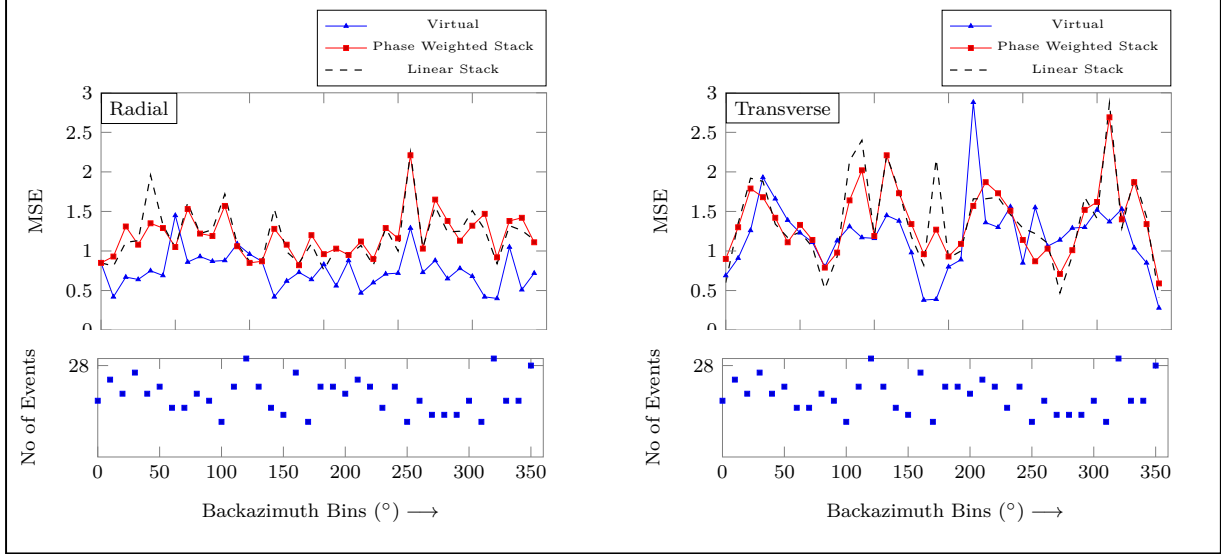


Figure 5: Mean-Square-Error (MSE) of virtual and stacked RFs w.r.t corresponding true RFs for Station 1 (Model 1). MSE of virtual RFs are consistently lower than that of stacked RFs

5.2 Virtual RFs

The virtual RFs were generated following Eq. 17. To achieve good quality results, we selected an earthquake with a high magnitude and SNR, and subsequently applied mean-subtraction to these virtual RFs. To compare our method with conventional stacking, we also computed the stacked RFs in each bin. All RFs were bandpass filtered between 0.01 to 1.0 Hz. Fig. 9 and Fig. 10 show station-wise plots of linearly stacked, phase-weighted stacked, and virtual RFs, organized by increasing epicentral distance bins. These RFs are from all bins with the backazimuth bin range 296° to 304° . The virtual RFs generated are largely in alignment compared to Bloch et al. [2023] and Audet et al. [2009], although they exhibit notably enhanced SNR. For example, virtual RFs delineate the crustal structure in the subduction zone far better than linear-stacked RFs. Bloch et al. [2023] parameterized the subducting Juan de Fuca plate as a slab with three velocity interfaces: a negative velocity contrast at the top and two positive velocity contrasts below. In Fig. 9, the converted seismic phases reported by Bloch et al. [2023] (see Tab. 3) from the subducting slab (highlighted by colored lines) are exhibited clearly and consistently across the stations in the virtual RFs. The virtual radial RFs in the stations are comparable with those reported by Bloch et al. [2023]. Additionally, our approach was able to produce more number of RFs across varying backazimuths and epicentral distances, and effectively delineated the forward-scattered S-waves (between 0 to 10 s) more accurately than the RFs calculated by Bloch et al. [2023] (see supplementary material). Note that P_1S phases in the stations, TWKB, MCGB, KELB and KLNB, are not clearly interpretable in stacked RFs but are significantly enhanced in virtual RFs. In all stations, P_pS and P_mS phases, which originated from the middle velocity contrast and bottom velocity contrast (Moho), are properly resolved in time in virtual RFs, unlike in stacked RFs. The virtual RFs are also consistent across epicentral bins at each station, which is not the case in stacked RFs due to distortion by nuisance effects. Furthermore, virtual RFs show significant improvement in extracting crustal effects in transverse RFs, which is difficult to achieve by conventional RF technique because of the low SNR of the transverse component. Fig. 10 shows virtual transverse RFs in all stations with superior quality and consistency compared to stacked RFs.

We anticipate that future research focused on the interpretation and inversion of these enhanced virtual RFs will yield significant advancements in teleseismic imaging and crustal structure determination.

5.3 Sanity Checks

It is important to develop metrics and evaluations to assess the quality and effectiveness of signals generated by networks for accuracy, reliability, and real-world applicability. We perform the following sanity checks on the virtual RFs to ensure the validity and reliability of our methodology.

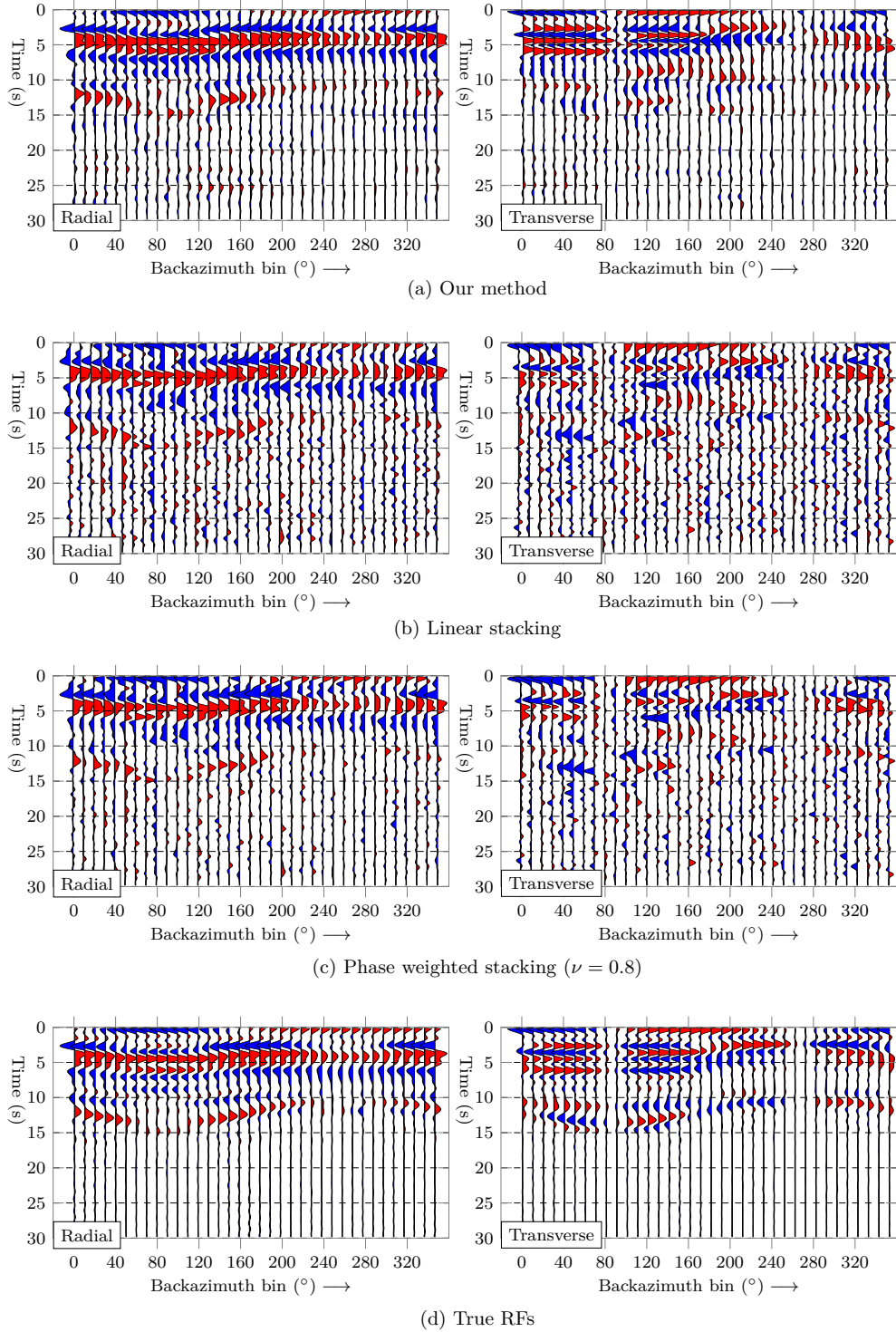


Figure 6: This figure shows radial and transverse RFs from all backazimuth bins for Station 1 (Model 2). a) Virtual RFs from the proposed method. b) RFs after bin-wise linear stacking. c) RFs after bin-wise phase-weighted stacking (PWS). Virtual RFs resemble the true RF more closely than the stacked RFs. Note that no P phase at $t = 0$ is observed in all RFs due to the mean-subtraction.

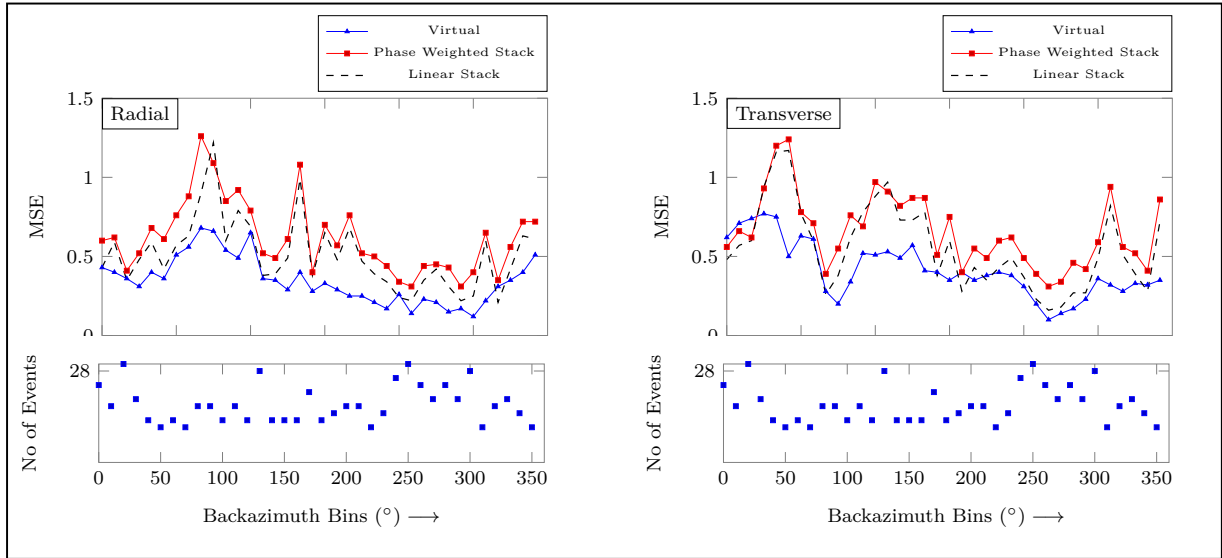


Figure 7: Similar to Fig. 5, but for the synthetic model in Tab. 2.

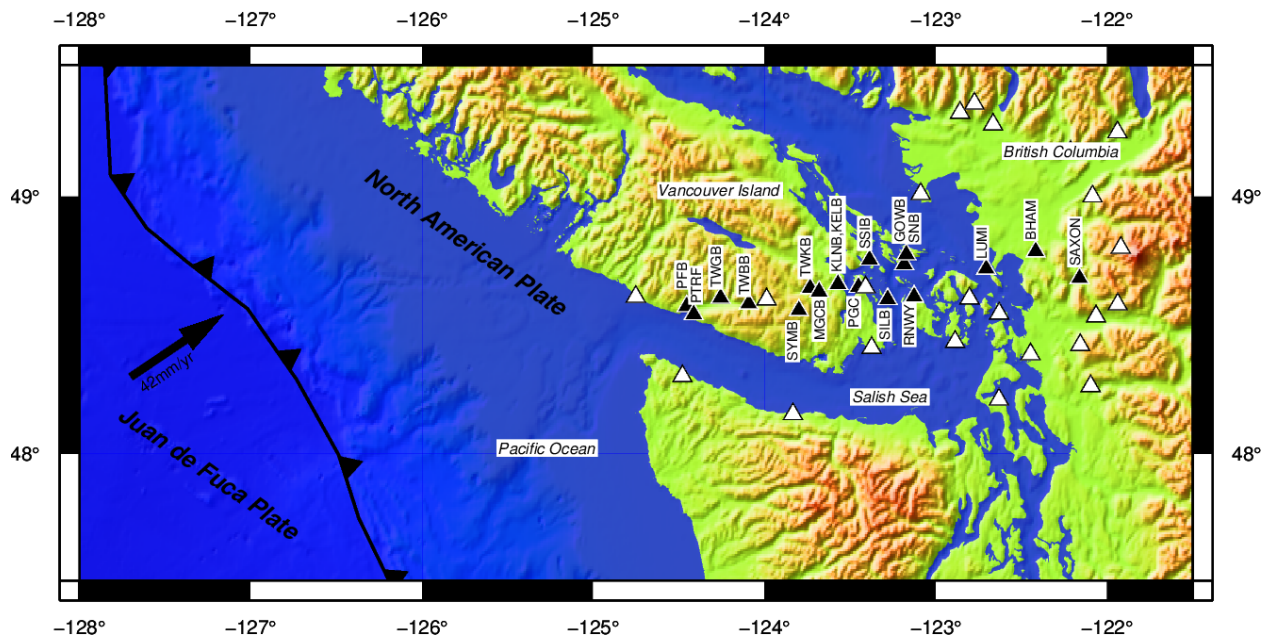


Figure 8: Map illustrating the tectonic setting and positions of the stations (represented by black and white triangles) utilized in the study. This map also depicts the subduction of the Juan de Fuca plate beneath the North American plate, occurring at a rate of 42 mm/yr [DeMets et al., 1994] (indicated by a black arrow). The solid black line adorned with triangles marks the subduction boundary. Stations are from the POLARIS [Geological Survey of Canada, 2000], C8 [Geological Survey of Canada, 2002], CN [Natural Resources Canada, 1975], and UW [University of Washington, 1963] networks. While all stations are utilized for training, this paper specifically plots the receivers marked by black triangles that are approximately positioned along a transect.

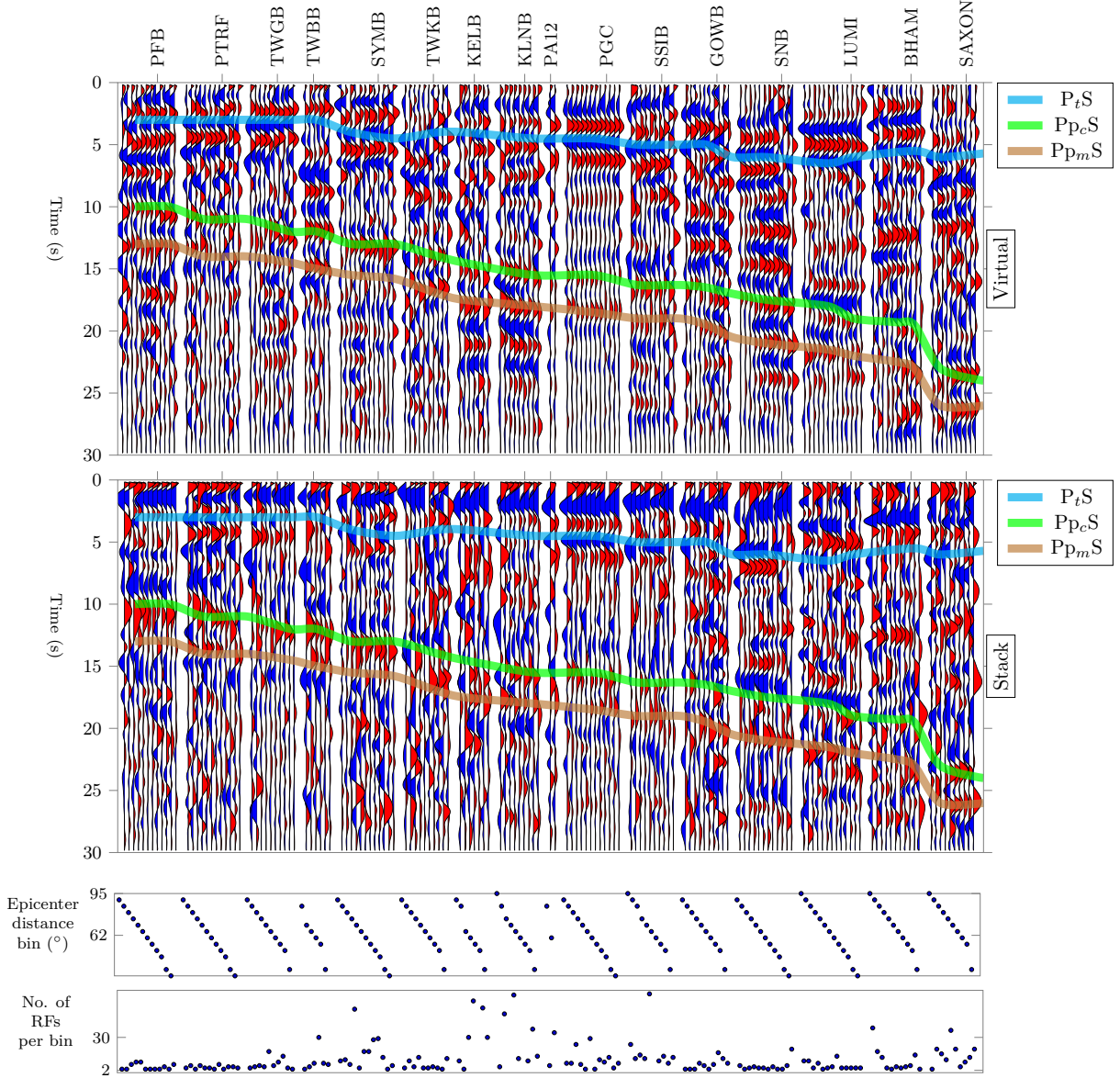


Figure 9: Virtual and linear stacked radial RFs at seismic stations transversing the Cascadia subduction zone. Key seismic phases (highlighted by colored lines) are more clear and resolved in the virtual RFs than in stacked RFs. The notation for these phases follows Bloch et al. [2023], as given in Tab. 3. Note that there is no P-wave at $t = 0$ for virtual RFs due to mean-subtraction. A reasonable correspondence between the virtual RFs and the raw RFs serves as a verification that the network-produced virtual RFs are physically credible.

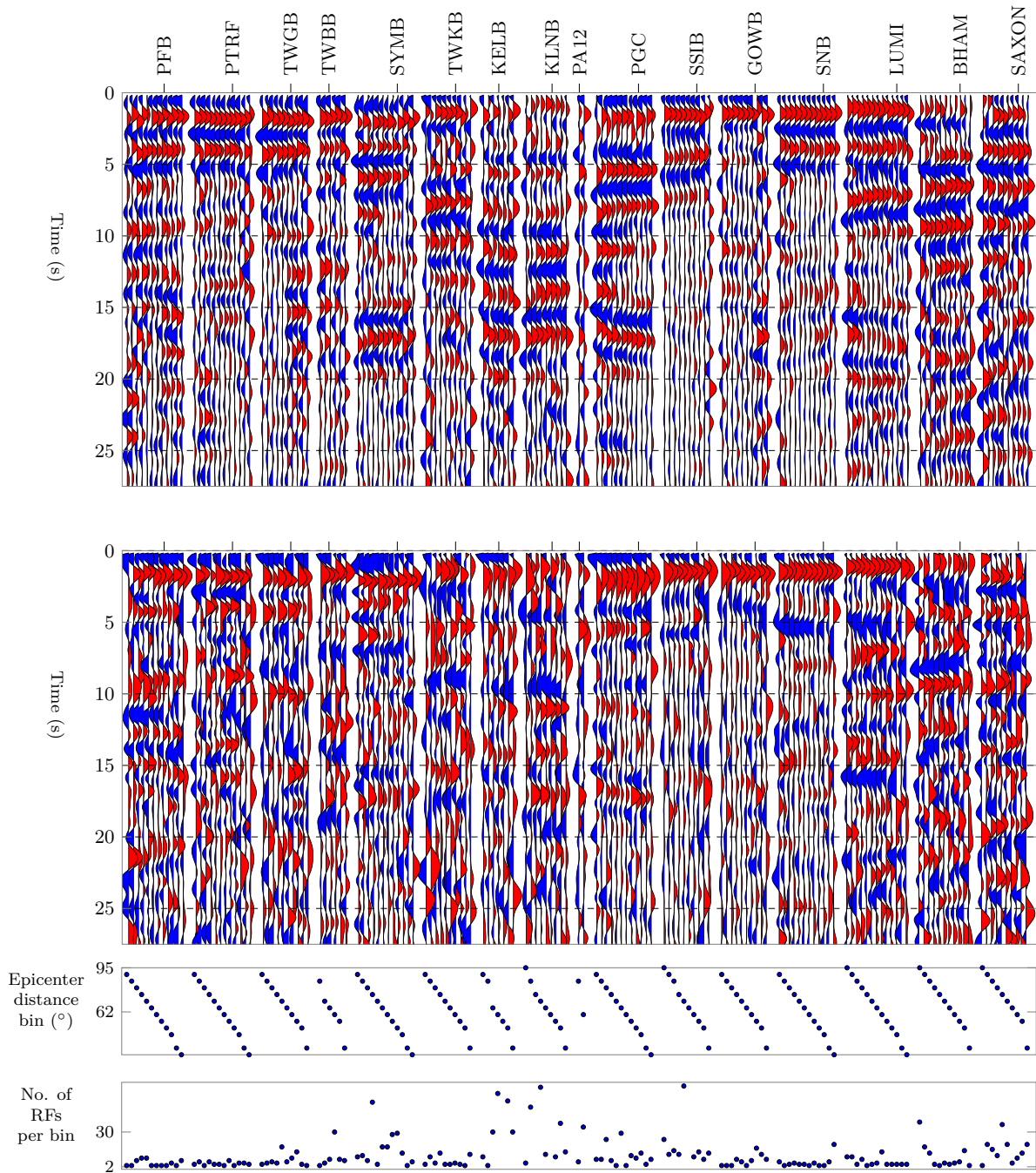


Figure 10: Similar to Fig. 9, but pertaining to transverse RFs. It is important to observe that the virtual RFs exhibit greater complexity and enhancement, allowing for the converted phases to be smoothly traced along the transect. A reasonable correspondence between the virtual RFs and the raw RFs serves as a verification that the network-produced virtual RFs are physically credible.

1. SymAE independently extracts coherent crustal effects from each data point, indicating that there can be substantial variations in crustal effects between any two data points. However, the virtual RFs from nearby stations (PFB and PTRF), as well as the RFs from stations located at the same site (KELB and KLNB), exhibit a strong similarity. Moreover, the physics governing wave propagation indicates that gradual changes in crustal effects with backazimuth and epicentral distance, as demonstrated in the synthetic RFs in Fig. 1, are predictable. Consistent with this, as shown in Fig. 9 and Fig. 10, the virtual RFs in various epicentral bins at all stations exhibit smooth variations. This consistency confirms our method’s ability to extract true crustal effects rather than random anomalies.
2. The crustal effects of virtual RFs, generated by various earthquakes that occur at similar locations, are expected to be analogous. To confirm this, we divided the earthquakes in one bin into two distinct groups and train the model separately for each group. After training was performed, the virtual RFs for both groups displayed a remarkable level of similarity, evidenced by a low mean square error.

These checks confirm that the SymAE results are physically plausible.

6 Discussion

In this study, we propose a novel method for separating nuisance effects from RFs. Unlike conventional synthetic experiments for RF denoising, which typically add Gaussian noise to noise-free synthetic RFs, our method introduces Gaussian noise to synthetic seismograms before applying frequency domain deconvolution. This approach results in more realistic non-Gaussian nuisance effects. Previous studies [Dalai et al., 2021, Olugboji et al., 2023, Dokht et al., 2016] have employed sparsity constraints to suppress nuisance effects; however, these approaches fall short because the nuisance effects are non-Gaussian signals produced during deconvolution. Our approach employs symmetric autoencoders to learn a disentangled representation of RFs, allowing for the effective separation of nuisance effects. The results of our synthetic RF experiments (see Fig. 4 and Fig. 6) demonstrate that while conventional stacking is ineffective, our technique effectively separates crustal effects from nuisance effects, significantly improving RF denoising.

Earthquakes typically occur in specific tectonically active regions, resulting in a nonuniform distribution of teleseismic earthquakes in terms of backazimuth and epicentral distance at seismic stations. This leads to substantial variability in the number of RFs per bin, causing inconsistency in RF stacking and unreliable measurement of S-wave variation across bins. In our synthetic experiments, the count of RFs in a bin was randomly varied between 15 and 30. Despite these variations, virtual RFs (refer to Fig. 4 and 6) exhibit consistency along backazimuth. Similarly, at seismic stations in the Cascadia Subduction Zone, both radial and transverse virtual RFs (refer to Fig. 9 and Fig. 10) consistently show stability across epicentral distances, regardless of variations in the number of RFs per bin. Temporary seismic stations operate for limited durations and often capture fewer teleseismic earthquakes, leading to a reduced number of RFs per bin. Furthermore, filtering noisy seismograms further decreases the usable RF count, making RF analysis challenging. However, our method utilizes all available RFs, regardless of quality, enhancing their availability for analysis (see supplementary material). This makes our approach particularly suitable for temporary stations with a limited number of recorded teleseismic events.

As with any deep neural network, training the SymAE method requires a thoughtful selection of hyperparameters, with particular attention to the dropout rate and the length of the nuisance code (m), to achieve an effective disentanglement between nuisance and crustal effects during encoding. If the dropout rate is too high, it results in a higher reconstruction loss. A lengthy nuisance code causes the decoder to concentrate excessively on the inference of nuisance encoder, thereby ignoring coherent encoder, which impedes disentanglement. On the other hand, too short nuisance code can lead to overfitting, making the network unstable. Therefore, selecting optimal hyperparameters is crucial for disentanglement while maintaining the reconstruction fidelity of RFs. Synthetic experiments are conducted to refine the SymAE network architecture. The same networks applied to synthetic RF datasets are employed for real RF datasets without alteration. This is promising and suggests that our approach is not particularly sensitive to the choice of architecture.

This study assumes that the crustal effects across RFs within a bin or data point are coherent. It means that converted seismic waves, originating from the crustal structures due to distant earthquakes within a bin, have comparable raypaths and minimal travel-time differences. This coherence is essential for the SymAE network to learn the disentangled representation of the RFs and separate the crustal and nuisance effects effectively. The validity of this assumption is influenced by the size of the bin, how the earthquakes are grouped, and the depth of the receiver-side structure being examined. For successful extraction of converted seismic waves from the crust or mantle, the bin size should be such that travel-time differences within the bin are insignificant. Travel-time discrepancies grow as deeper mantle structures are examined. Although this technique is primarily optimized for examining crustal effects near the receiver, it can also be adapted for investigating deeper structures with meticulous selection of the bin size.

7 Conclusions

Receiver functions (RFs) are an essential technique for analyzing crust and mantle structures beneath seismic stations; however, they are often contaminated with pseudorandom nuisance effects that reduce the precision and reliability of RF measurements. We introduce an innovative approach to removing these unwanted nuisance effects from RFs through an unsupervised deep learning framework using symmetric autoencoders. This method effectively disentangled the nuisance effects from crustal effects, allowing the generation of virtual RFs with similar nuisance effects, and averaged them out to remove the common nuisance effects. Our approach outperforms linear stacking and phase-weighted stacking in denoising synthetic RFs, which are affected by realistic non-Gaussian nuisance effects, resulting in high-quality and consistent RFs. Unlike stacked RFs, the polarity reversal in transverse RFs along the backazimuth is clearly depicted in virtual RFs. The application of our method in RFs from seismic stations at the Cascadia Subduction Zone's forearc has shown strong agreement with previous studies. Our method better delineated the various layers of the subducting slab and enhanced the crustal effects, which were not as clear in linearly stacked RFs. Virtual RFs demonstrated consistency across backazimuth, epicentral distances, and nearby stations. The method was proved robust by integrating all available RFs, regardless of their signal quality. The automated and human-free process of our method provides both scalability and reproducibility. The compelling results of this study suggest that our approach can greatly improve RF analysis by eliminating nuisances, enabling more precise interpretations of crustal and mantle structures, and revealing new insights previously obscured by noisy RFs, thereby advancing teleseismic imaging and solid-Earth studies.

Acknowledgments This work is funded by the Science and Engineering Research Board, Department of Science and Technology, India (Grant Number SRG/2021/000205). This study was enabled by Julia and Python programming languages. Flux package [Innes et al., 2018] was used to model and train neural networks. Data were downloaded from IRIS Data Center and Natural Resources Canada Data Center using ObsPyDMT [Hosseini and Sigloch, 2017].

Data Availability

Earthquake waveform data used in this study are available in IRIS Data Center and Natural Resources Canada Data Center.

References

- Vadim Levin, Steven Roecker, Peter Graham, and Ali Hosseini. Seismic anisotropy indicators in western tibet: Shear wave splitting and receiver function analysis. *Tectonophysics*, 462(1):99–108, 2008. doi:10.1016/j.tecto.2008.03.019.
- Martha K. Savage, J. Park, and H. Todd. Velocity and anisotropy structure at the hikurangi subduction margin, new zealand from receiver functions. *Geophysical Journal International*, 168(3):1034–1050, March 2007. doi:10.1111/j.1365-246X.2006.03086.x.
- Zhen Liu, Jeffrey Park, and Danny M Rye. Crustal anisotropy in northeastern tibetan plateau inferred from receiver functions: Rock textures caused by metamorphic fluids and lower crust flow? *Tectonophysics*, 661:66–80, 2015. doi:10.1016/j.tecto.2015.08.006.
- D. E. McNamara and T. J. Owens. Azimuthal shear-wave velocity anisotropy in the basin and range province using moho ps converted phases. *Journal of Geophysical Research*, 98(B7):12003–12017, 1993. doi:10.1029/93JB00711.
- I. Bianchi, J. Park, N. Piana Agostinetti, and V. Levin. Mapping seismic anisotropy using harmonic decomposition of receiver functions: An application to northern apennines, italy. *Journal of Geophysical Research*, 115:B12317, 2010. doi:10.1029/2009JB007061.
- T. Zheng, Z. Ding, J. Ning, L. Chang, X. Wang, and F. et al. Kong. Crustal azimuthal anisotropy beneath the southeastern tibetan plateau and its geodynamic implications. *Journal of Geophysical Research: Solid Earth*, 123:9733–9749, 2018. doi:10.1029/2018JB015995.
- Katsuhiko Shiomi and Jeffrey Park. Structural features of the subducting slab beneath the kii peninsula, central japan: Seismic evidence of slab segmentation, dehydration, and anisotropy. *Journal of Geophysical Research: Solid Earth*, 113(B10), 2008. doi:https://doi.org/10.1029/2007JB005535. URL https://agupubs.onlinelibrary.wiley.com/doi/abs/10.1029/2007JB005535.
- Lupei Zhu and Hiroo Kanamori. Moho depth variation in southern california from teleseismic receiver functions. *Journal of Geophysical Research: Solid Earth*, 105(B2):2969–2980, 2000.
- J. Kolb and V. Lekić. Receiver function deconvolution using transdimensional hierarchical bayesian inference. *Geophysical Journal International*, 197(3):1719–1735, 2014.

- T. Akuhara, M. G. Bostock, A. P. Plourde, and M. Shinohara. Beyond receiver functions: Green's function estimation by transdimensional inversion and its application to obs data. *Journal of Geophysical Research: Solid Earth*, 124(2):1944–1961, 2019. doi:10.1029/2018JB016499.
- J. Park and V. Levin. Receiver functions from multiple-taper spectral correlation estimates. *Bull. Seism. Soc. Am.*, 90(6):1507–1520, 2000.
- Q. Zhang, Y. Chen, F. Zhang, and Y. Chen. Improving receiver function imaging with high-resolution radon transform. *Geophysical Journal International*, 230(2):1292–1304, March 2022. doi:10.1093/gji/ggac116.
- Ziqi Zhang and Tolulope Olugboji. Crustal imaging with noisy teleseismic receiver functions using sparse radon transforms. *Bulletin of the Seismological Society of America*, 114(3):1600–1612, 2024. doi:10.1785/0120230254.
- H. P. Crotwell and T. J. Owens. Automated receiver function processing. *Seismological Research Letters*, 76(6):702–709, 2005. doi:10.1785/gssrl.76.6.702.
- Xiaoning Yang, Gary L. Pavlis, and Yibo Wang. A quality control method for teleseismic p-wave receiver functions. *Bulletin of the Seismological Society of America*, 106(5):1948–1962, 2016. doi:10.1785/0120150347.
- C. Gong, L. Chen, Z. Xiao, and X. Wang. Deep learning for quality control of receiver functions. *Frontiers in Earth Science*, 2022. doi:10.3389/feart.2022.921830.
- H. E. Krueger, I. Gama, and K. M. Fischer. Global patterns in cratonic mid-lithospheric discontinuities from sp receiver functions. *Geochemistry, Geophysics, Geosystems*, 22(6), 2021. doi:10.1029/2021GC009819.
- S. Sabermahani and A. Frederiksen. Deeprfqc: automating quality control for p-wave receiver function analysis using a u-net inspired network. *Seismica*, 3(2), 2024. doi:10.26443/seismica.v3i2.1341.
- H. Gurrola, G. E. Baker, and J. B. Minster. Simultaneous time domain deconvolution with application to the computation of receiver functions. *Geophys. J. Int.*, 120:537–543, 1995.
- V. Levin and J. Park. Crustal anisotropy beneath the ural mtns foredeep from teleseismic receiver functions. *Geophys. Res. Lett.*, 24:1283–1286, 1997.
- Jiafu Hu, Haiyan Yang, Guangquan Li, and Hengchu Peng. A review on the analysis of the crustal and upper mantle structure using receiver functions. *Journal of Asian Earth Sciences*, 111:589–603, 2015. ISSN 1367-9120. doi:10.1016/j.jseaes.2015.06.007.
- W. Bloch, M. G. Bostock, and P. Audet. A cascadia slab model from receiver functions. *Geochemistry, Geophysics, Geosystems*, 24(10):e2023GC011088, 2023. doi:10.1029/2023GC011088.
- Y. Ozakin and Y. Ben-Zion. Systematic receiver function analysis of the moho geometry in the southern california plate-boundary region. *Pure and Applied Geophysics*, 172:1167–1184, 2015. doi:10.1007/s00024-014-0924-6.
- M. Schimmel and H. Paulssen. Noise reduction and detection of weak, coherent signals through phase-weighted stacks. *Geophysical Journal International*, 130:497–505, 1997.
- T. Olugboji, Z. Zhang, S. Carr, C. Ekmekci, and M. Cetin. On the detection of upper mantle discontinuities with radon-transformed ps receiver functions (crisp-rf), June 2023.
- Yan Chen, Jian Chen, Bengang Guo, Shuyun Qi, and Ping Zhao. Denoising the receiver function through curvelet transforming and migration imaging. *Chinese Journal of Geophysics*, 62(6):2027–2037, 2019.
- R. M. H. Dokht, Y. J. Gu, and M. D. Sacchi. Singular spectrum analysis and its applications in mapping mantle seismic structure. *Geophysical Journal International*, 208(3):1430–1442, December 2016. doi:10.1093/gji/ggw473.
- F. Wang, X. Song, and J. Li. Deep learning-based $h - \kappa$ method (hknet) for estimating crustal thickness and vp/vs ratio from receiver functions. *Journal of Geophysical Research: Solid Earth*, 127(6), June 2022. doi:10.1029/2022jb023944.
- L. Zhu. Crustal structure across the san andreas fault, southern california from teleseismic converted waves. *Earth planet. Sci. Lett.*, 179:183–190, 2000.
- Tian-Yu Zheng, Liang Zhao, Yu-Mei He, and Ri-Xiang Zhu. Seismic imaging of crustal reworking and lithospheric modification in eastern china. *Geophysical Journal International*, 196(2):656–670, February 2014. doi:10.1093/gji/ggt420.
- Pascal Vincent, Hugo Larochelle, Yoshua Bengio, and Pierre-Antoine Manzagol. Extracting and composing robust features with denoising autoencoders. In *Proceedings of the 25th International Conference on Machine Learning*, pages 1096–1103. ACM, 2008.
- B. Dalai, P. Kumar, U. Srinu, and M. K. Sen. De-noising receiver function data using the unsupervised deep learning approach. *Geophysical Journal International*, 229(2):737–749, December 2021. doi:10.1093/gji/ggab494.

- Omar M. Saad and Yangkang Chen. A fully-unsupervised and highly-generalized deep learning approach for random noise suppression. *Geophysical Prospecting*, 2020. doi:10.1111/1365-2478.13062.
- M. Ranzato, F. J. Huang, Y. L. Boureau, and Y. LeCun. Unsupervised learning of invariant feature hierarchies with applications to object recognition. In *2007 IEEE Conference on Computer Vision and Pattern Recognition*, pages 1–8, Minneapolis, MN, USA, 2007. doi:10.1109/CVPR.2007.383157.
- Alireza Makhzani, Jonathon Shlens, Navdeep Jaitly, Ian J Goodfellow, and Brendan Frey. Adversarial autoencoders. *International Conference on Learning Representations Workshop*, 2015.
- Diane Bouchacourt, Ryota Tomioka, and Sebastian Nowozin. Multi-level variational autoencoder: Learning disentangled representations from grouped observations. *Proceedings of the AAAI Conference on Artificial Intelligence*, 32, 05 2017. doi:10.1609/aaai.v32i1.11867.
- Michael F Mathieu, Junbo Jake Zhao, Junbo Zhao, Aditya Ramesh, Pablo Sprechmann, and Yann LeCun. Disentangling factors of variation in deep representation using adversarial training. *Advances in Neural Information Processing Systems*, 29, 2016. URL https://proceedings.neurips.cc/paper_files/paper/2016/file/ef0917ea498b1665ad6c701057155abe-Paper.pdf.
- Pawan Bharadwaj, Matthew Li, and Laurent Demanet. Redatuming physical systems using symmetric autoencoders. *Phys. Rev. Res.*, 2(2):023118, May 2022. doi:10.1103/PhysRevResearch.4.023118.
- T. Nicholson, M. Bostock, and J. F. Cassidy. New constraints on subduction zone structure in northern cascadia. *Geophysical Journal International*, 161(3):849–859, June 2005. doi:10.1111/j.1365-246X.2005.02605.x.
- Pascal Audet, Michael G. Bostock, Norman I. Christensen, and Sheila M. Peacock. Seismic evidence for overpressured subducted oceanic crust and megathrust fault sealing. *Nature*, 457(7225):76–78, 2009. doi:10.1038/nature07650.
- Benoit Tauzin, Thanh-Son Pham, and Hrvoje Tkalčić. Receiver functions from seismic interferometry: a practical guide. *Geophysical Journal International*, 217(1):1–24, April 2019. doi:10.1093/gji/ggz002.
- Wasja Bloch and Pascal Audet. Pyraysum: Software for modeling ray-theoretical plane body-wave propagation in dipping anisotropic media. *Seismica*, 2(1), Feb. 2023. doi:10.26443/seismica.v2i1.220. URL <https://seismica.library.mcgill.ca/article/view/220>.
- Geoffrey E Hinton and Ruslan R Salakhutdinov. Reducing the dimensionality of data with neural networks. *Science*, 313:504–507, 2006.
- Andrew Ng. Sparse autoencoder. *CS294A Lect. Notes*, 72:1–19, 2011.
- Kurt Hornik, Maxwell Stinchcombe, and Halbert White. Multilayer feedforward networks are universal approximators. *Neural Networks*, 2(5):359–366, 1989. doi:10.1016/0893-6080(89)90020-8.
- George Cybenko. Approximation by superpositions of a sigmoidal function. *Mathematics of Control, Signals and Systems*, 2(4):303–314, 1989. doi:10.1007/BF02551274.
- Manzil Zaheer, Satwik Kottur, Siamak Ravanbakhsh, Barnabás Póczos, Ruslan Salakhutdinov, and Alexander J. Smola. Deep sets. *Advances in Neural Information Processing Systems*, pages 3392–3402, Apr 2017. ISSN 10495258. URL <http://arxiv.org/abs/1703.06114>.
- Sida Wang and Christopher Manning. Fast dropout training. *International Conference on Machine Learning*, pages 118–126, 2013.
- Durk P Kingma, Tim Salimans, and Max Welling. Variational dropout and the local reparameterization trick. In *Advances in neural information processing systems*, volume 28, pages 2575–2583, 2015.
- Nitish Srivastava, Geoffrey Hinton, Alex Krizhevsky, Ilya Sutskever, and Ruslan Salakhutdinov. Dropout: A simple way to prevent neural networks from overfitting. *The journal of machine learning research*, 15(1):1929–1958, 2014.
- Alex Krizhevsky, Ilya Sutskever, and Geoffrey E Hinton. Imagenet classification with deep convolutional neural networks. In *Advances in neural information processing systems*, volume 25, pages 1097–1105, 2012.
- J.F. Cassidy. A comparison of the receiver structure beneath stations of the canadian national seismograph network. *Canadian Journal of Earth Sciences*, 32:938–951, 1995.
- C. A. Langston. Structure under mount rainier, washington, inferred from teleseismic body waves. *J. Geophys. Res.*, 84: 4749–4762, 1979.
- Geological Survey of Canada. Portable observatories for lithospheric analysis and research investigating seismicity, 2000. URL <https://www.fdsn.org/networks/detail/P0/>.
- Geological Survey of Canada. Canadian seismic research network, 2002. URL <https://www.fdsn.org/networks/detail/C8/>.

- Natural Resources Canada. Canadian national seismograph network, 1975. URL <https://www.fdsn.org/networks/detail/CN/>.
- University of Washington. Pacific northwest seismic network - university of washington, 1963. URL <https://www.fdsn.org/networks/detail/UW/>.
- Mijian Xu and Jing He. Seispy: Python module for batch calculation and postprocessing of receiver functions. *Seismological Research Letters*, 94(2A):935–943, 2022. doi:10.1785/0220220288.
- C. DeMets, R. G. Gordon, D. F. Argus, and S. Stein. Effect of recent revisions to the geomagnetic reversal time scale on estimates of current plate motions. *Geophysical Research Letters*, 21(20):2191–2194, 1994. doi:10.1029/94gl02118.
- Michael Innes, Elliot Saba, Keno Fischer, Dhairya Gandhi, Marco Concetto Rudilosso, Neethu Mariya Joy, Tejan Karmali, Avik Pal, and Viral Shah. Fashionable modelling with flux. *CoRR*, abs/1811.01457, 2018. URL <https://arxiv.org/abs/1811.01457>.
- K. Hosseini and K. Sigloch. Obspydmt: a python toolbox for retrieving and processing large seismological data sets. *Solid Earth*, 8:1047–1070, 2017. doi:10.5194/se-8-1047-2017.
- Robert W Clayton and Robert A Wiggins. Source shape estimation and deconvolution of teleseismic body waves. *J. R. Astr. Soc.*, 47:151–177, 1976.

A Calculation of RF

In this appendix, we show that the radial receiver function (RF) r from a single teleseismic earthquake can be expressed as follows:

$$r(t, \mathbf{p}) = \int_{\tau} s_a(t - \tau, \mathbf{p}) g^{r,z}(\tau, \mathbf{p}) d\tau + \epsilon(t, \mathbf{p}), \quad (\text{A.1})$$

Here, s_a represents a zero-phase signal, $g^{r,z}$ denotes the crustal impulse response, \mathbf{p} is the ray parameter, and ϵ accounts for noise terms. The radial receiver function (RF) is calculated by deconvolving the vertical component seismogram from the radial component seismogram as described in Eq. 1. Fourier transform converts the convolution in the time domain into multiplication in frequency domain. Deconvolution is the process of reversing the effects of convolution and thus can be expressed as a division in the frequency domain. We express the measured seismograms in frequency domain as

$$\begin{aligned} D^z(\omega, \mathbf{p}) &= S(\omega)G^z(\omega, \mathbf{p}) + \epsilon^z(\omega) \quad \text{and} \\ D^r(\omega, \mathbf{p}) &= S(\omega)G^r(\omega, \mathbf{p}) + \epsilon^r(\omega), \end{aligned} \quad (\text{A.2})$$

where ω is the angular frequency. Then, the radial receiver function is given by

$$R(\omega, \mathbf{p}) = \frac{D^r(\omega, \mathbf{p})D^z(\omega, \mathbf{p})^*}{|D^z(\omega, \mathbf{p})|^2},$$

where the complex conjugate of the vertical component is $D^z(\omega, \mathbf{p})^*$. It is important to recognize that the spectrum of D^z may contain zeros, causing instability. To address this issue, various regularization techniques can be employed. We represent the regularization factor by λ , which varies according to the chosen regularization method, resulting in

$$R(\omega, \mathbf{p}) = \lambda(\omega, \mathbf{p})D^r(\omega, \mathbf{p})D^z(\omega, \mathbf{p})^*. \quad (\text{A.3})$$

For example, in the case of water-level regularization [Clayton and Wiggins, 1976],

$$\lambda(\omega, \mathbf{p}) = \frac{W(\omega)}{\max(|D^z(\omega, \mathbf{p})|^2, c \max_{\omega}(|D^z(\omega, \mathbf{p})|^2))},$$

where c is the water-level parameter and $W(\omega) = \exp(-\frac{\omega}{4a^2})$ is a Gaussian filter with a width given by the parameter a .

By substituting Eq. A.2 into Eq. A.3, we derive

$$\begin{aligned} R(\omega, \mathbf{p}) &= \lambda(\omega, \mathbf{p}) (|S(\omega)|^2 G^r(\omega, \mathbf{p})G^z(\omega, \mathbf{p})^* + S(\omega)^* G^z(\omega, \mathbf{p})^* \epsilon^r(\omega) \\ &\quad + S(\omega)G^r(\omega, \mathbf{p})\epsilon^z(\omega)^* + \epsilon^r(\omega)\epsilon^z(\omega)^*). \end{aligned} \quad (\text{A.4})$$

In this expression, we have $\epsilon^r(\omega)\epsilon^z(\omega)^* = 0$, based on the assumption that the seismic noise from the radial and vertical components is uncorrelated. The term $G^r(\omega, \mathbf{p})G^z(\omega, \mathbf{p})^*$ denotes the radial crustal impulse response, whereas

$S(\omega)^* G^z(\omega, \mathbf{p})^* \varepsilon^r(\omega)$ and $S(\omega) G^r(\omega, \mathbf{p}) \varepsilon^z(\omega)^*$ account for nuisance from random noise in the seismogram. These nuisance effects are relatively insignificant for high-SNR seismograms but can significantly distort the radial crustal response in low-SNR seismograms. The amplification of seismic noise is influenced by the signature of the source within the regularization factor λ , which plays a role in the nuisance effects in the RF. Rewriting Eq. A.4 results in the following equation,

$$R(\omega, \mathbf{p}) = s_a(\omega, \mathbf{p}) G^{r,z}(\omega, \mathbf{p}) + \varepsilon(\omega, \mathbf{p}), \quad (\text{A.5})$$

where

$$\begin{aligned} G^{r,z}(\omega, \mathbf{p}) &= G^r(\omega, \mathbf{p}) G^z(\omega, \mathbf{p})^*, \\ s_a(\omega, \mathbf{p}) &= \lambda(\omega, \mathbf{p}) |S(\omega)|^2, \\ \varepsilon(\omega, \mathbf{p}) &= \lambda(\omega) S(\omega)^* G^z(\omega, \mathbf{p})^* \varepsilon^r(\omega) + \lambda(\omega) S(\omega) G^r(\omega, \mathbf{p}) \varepsilon^z(\omega)^*. \end{aligned}$$

Importantly, $s_a(\omega)$ represents a zero-phase signal, influenced by both the regularization method and the source signature. In the time domain, Eq. A.5 corresponds to Eq. A.1.

B Elimination of Additive Nuisance Using Mean Subtraction

This appendix begins by illustrating how RFs within a bin can be written as a sum of coherent crustal effects and nuisance effects specific to each RF. Subsequently, we examine a collection of virtual RFs, all generated with identical nuisance effects. We demonstrate that applying mean subtraction highlights the crustal effects. As discussed in Sec. 2.2, RFs from the j -th bin can be expressed as follows:

$$\mathbf{r}_j^{(i)}[t] = \sum_{\tau} s_a^{(i)}[\tau] \mathbf{g}_j^{r,z}[t - \tau] + \boldsymbol{\epsilon}^{(i)}[t], \quad \forall i, \quad (\text{B.1})$$

where i ranges from 1 to n_j and n_j represents the number of RFs in the j -th bin. The terms $s_a^{(i)}$ and $\boldsymbol{\epsilon}^{(i)}$ indicate the nuisance specific to the i -th RF in the j -th bin, while $\mathbf{g}_j^{r,z}$ signifies the common crustal response across all RFs in the j -th bin. The contribution from the term for $\tau = 0$ can be isolated, allowing us to express:

$$\mathbf{r}_j^{(i)}[t] = \underbrace{s_a^{(i)}[0] \mathbf{g}_j^{r,z}[t]}_{\text{Coherent; } \mathbf{c}_j[t]} + \underbrace{\sum_{\tau, \tau \neq 0} s_a^{(i)}[\tau] \mathbf{g}_j^{r,z}[t - \tau]}_{\text{Nuisance; } \mathbf{b}_j^{(i)}[t]} + \boldsymbol{\epsilon}^{(i)}[t], \quad \forall i. \quad (\text{B.2})$$

Considering that the RFs have been normalized, we disregard the variation in the auto-correlated source signal at $t = 0$, i.e., $s_a^{(i)}[0]$, with respect to i . Therefore, the term $s_a^{(i)}[0] \mathbf{g}_j^{r,z}[t]$ represents the coherent crustal effects. In contrast, the other terms vary among the RFs, indicating the nuisance effects. Hence, RFs within a bin or data point can be written as a combination of coherent crustal effects (\mathbf{c}_j) and specific nuisance effects ($\mathbf{b}_j^{(i)}$) unique to each RF. Here, the coherent crustal effects are specific to the j -th bin, and the nuisance effects are specific to the i -th RF within the bin.

As discussed in Sec. 3, SymAE has the ability to learn disentangled latent representation of RFs within a datapoint (bin). The latent coherent and nuisance codes specifically encode the crustal and nuisance effects, respectively. In Sec. 3.4, we illustrated how the swapping of latent codes enables the generation of a set of virtual receiver functions, represented as $\mathbf{V}_k^{(2)}$ (Eq. 17). RFs in $\mathbf{V}_k^{(2)}$ can be written using the coherent code (\mathbf{P}) and nuisance code (\mathbf{N}) as follows:

$$\mathbf{v}_{j,k}^{(2)} = \text{Dec}([\mathbf{P}_j; \mathbf{N}_k^{(2)}]), \quad \forall j, \quad (\text{B.3})$$

where j covers the range $1, 2, 3, \dots, N_b$ and N_b indicates the total number of bins across all stations. These virtual RFs retain the same nuisance effects due to the same nuisance code ($\mathbf{N}_k^{(2)}$) but exhibit different crustal effects. Employing Eq. B.2, the virtual RFs within the collection $\mathbf{V}_k^{(2)}$ can be written as:

$$\mathbf{v}_{j,k}^{(2)}[t] \approx \mathbf{c}_j[t] + \mathbf{b}_k^{(2)}[t], \quad \forall j. \quad (\text{B.4})$$

We used an approximate sign because this is our interpretation of how SymAE generates virtual RFs.

To eliminate the common nuisance effects, we subtract the mean of all RFs in $\mathbf{V}_k^{(2)}$ from each individual RFs, resulting in mean-subtracted RFs given by

$$\mathbf{v}_j[t] = \mathbf{v}_{j,k}^{(2)}[t] - \frac{1}{N_b} \sum_{j=1}^{N_b} \mathbf{v}_{j,k}^{(2)}[t], \quad \forall j. \quad (\text{B.5})$$


Substituting Eq. B.4 in Eq. B.5, we get


$$\mathbf{v}_j[t] \approx \mathbf{c}_j[t] - \frac{1}{N_b} \sum_{j=1}^{N_b} \mathbf{c}_j[t], \quad \forall j. \quad (\text{B.6})$$

Therefore, the mean-subtraction operation effectively removes the common nuisance effects. Now, assuming that the crustal structure varies across stations, the mean crustal effects between stations, i.e., $\frac{1}{N_b} \sum_{j=1}^{N_b} \mathbf{c}_j$, becomes negligible, except at the P-wave phase (at $t = 0$). Thus, apart from the crustal phases that remain coherent across all stations (or data points), each individual element in the set $\{\mathbf{v}_j \mid 1 \leq j \leq N_b\}$ emphasizes the crustal effects unique to the j -th bin. It is important to note that the mean-subtraction process removes the coherent P-wave phase present at $t = 0$ from these virtual RFs.

ENHANCED RECEIVER FUNCTION IMAGING OF CRUSTAL STRUCTURES USING SYMMETRIC AUTOENCODERS

A PREPRINT

 **T. Rengneichuonng Koireng**
Centre for Earth Sciences
Indian Institute of Science
Bengaluru, India 560012
tienterk@iisc.ac.in

 **Pawan Bharadwaj**
Centre for Earth Sciences
Indian Institute of Science
Bengaluru, India 560012
pawan@iisc.ac.in

November 22, 2024

Supplementary material

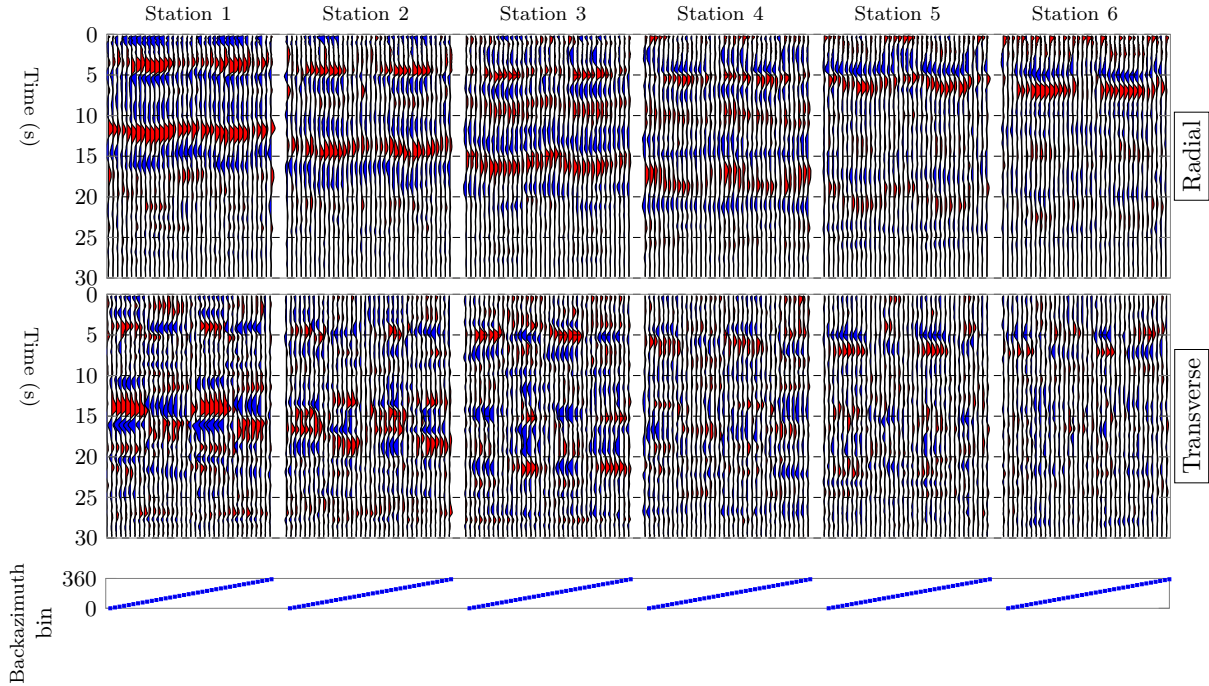


Figure 1: Virtual RFs for all stations (Synthetic experiment Model 1). All RFs are from same epicentral bin ($40^\circ - 50^\circ$) across all backazimuth bins. Note that there is no P arrival at $t = 0$ due to the *mean-subtraction*.

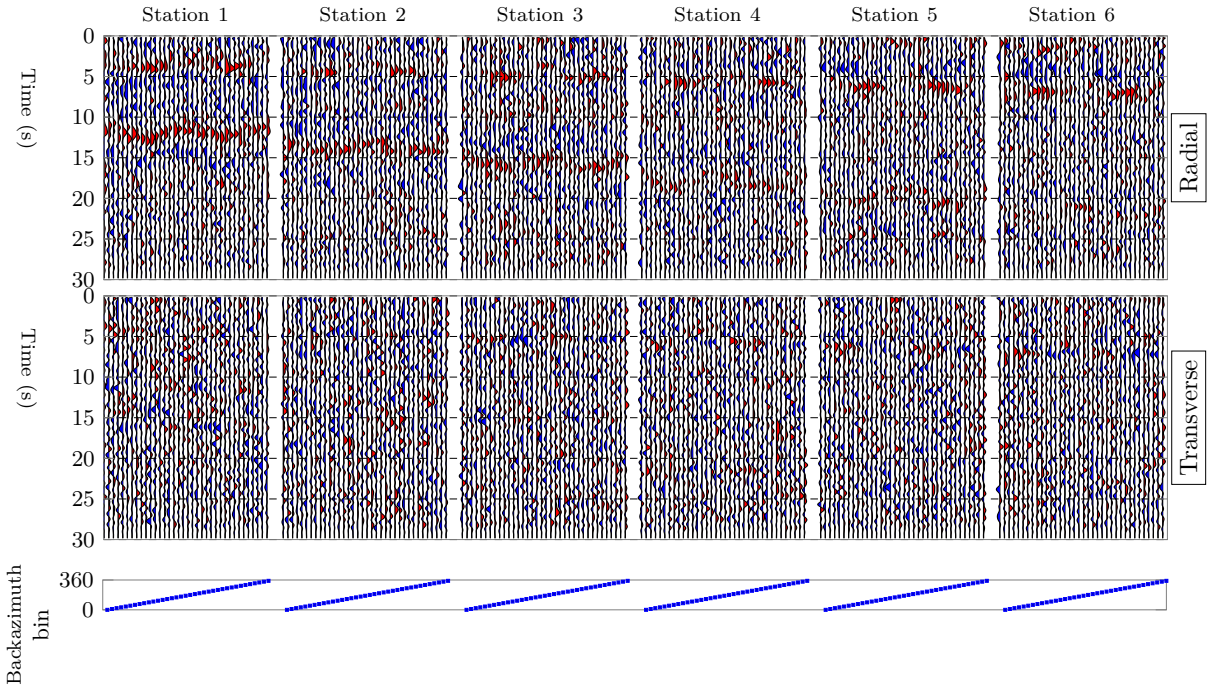


Figure 2: Bin-wise linear stacked RFs for all stations (Synthetic experiment Model 1). All RFs are from same epicentral bin ($40^\circ - 50^\circ$), across all backazimuth bins. Note that there is no P arrival at $t = 0$ due to the *mean-subtraction*.

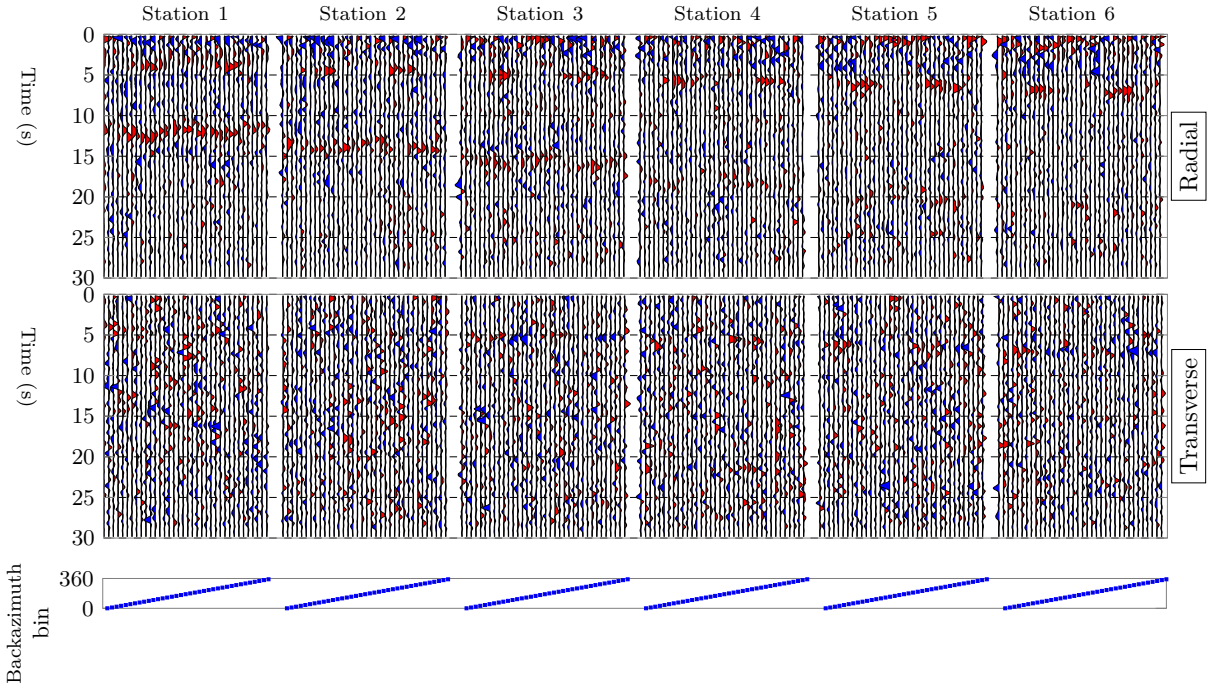


Figure 3: Bin-wise phase-weighted-stacked RFs for all stations (Synthetic experiment Model 1). $\nu = 0.8$. All All RFs are from same epicentral bin ($40^\circ - 50^\circ$), across all backazimuth bins. Note that there is no P arrival at $t = 0$ due to the *mean-subtraction*.

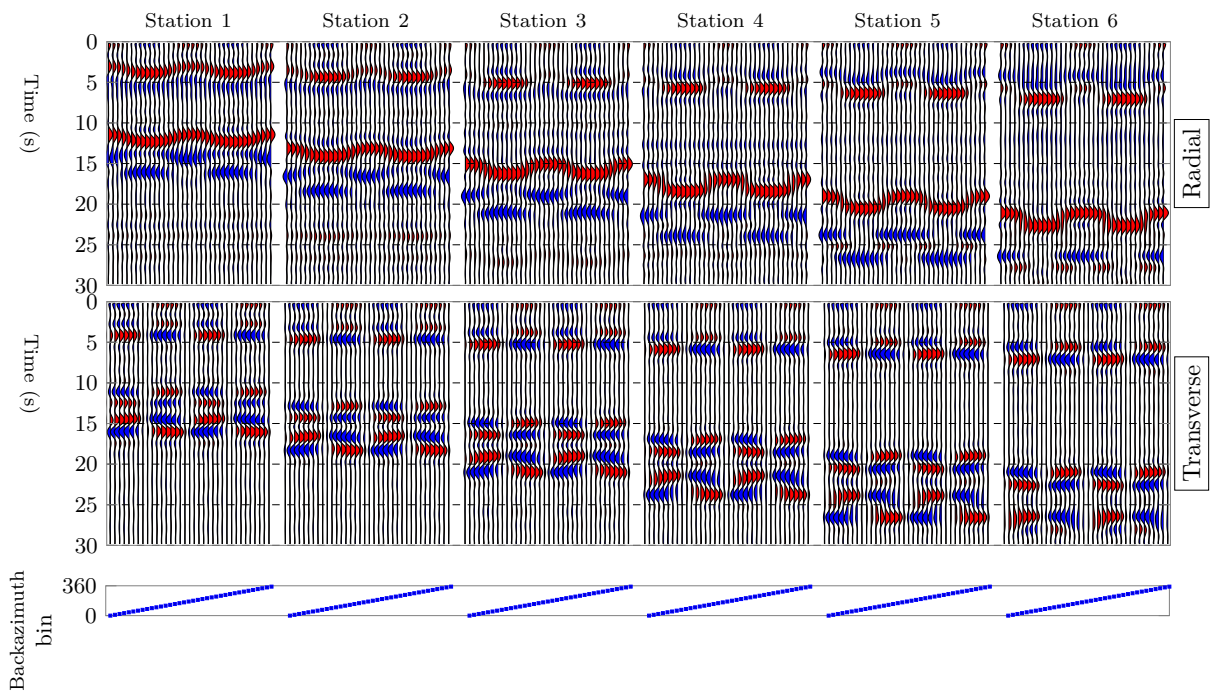


Figure 4: True RFs for all stations (Synthetic experiment Model 1). All RFs are from same epicentral bin ($40^\circ - 50^\circ$), across all backazimuth bins. Note that there is no P arrival at $t = 0$ due to the *mean-subtraction*.

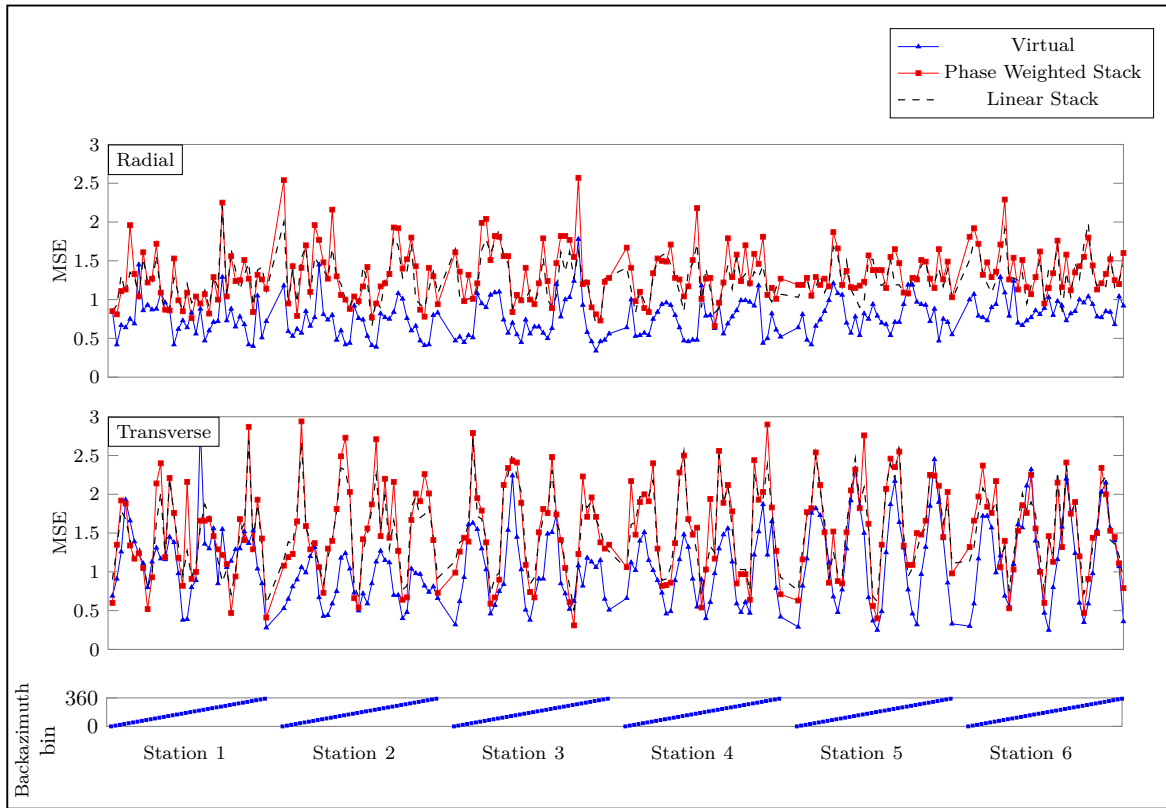


Figure 5: Mean Square Error (MSE) of virtual, linear stacked and phase-weighted-stacked RFs w.r.t corresponding true RFs for all stations (Model 1).

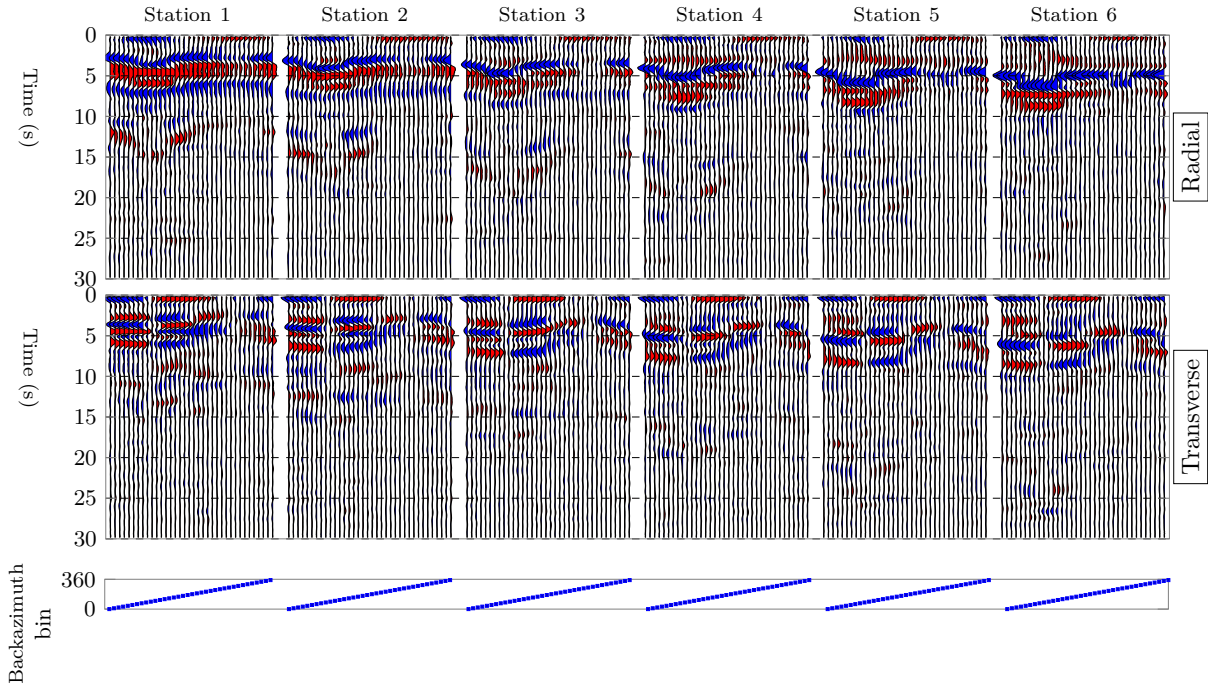


Figure 6: Virtual RFs for all stations (Synthetic experiment Model 1). All RFs are from same epicentral bin ($40^\circ - 50^\circ$), across all backazimuth bins. Note that there is no P arrival at $t = 0$ due to the *mean-subtraction*.

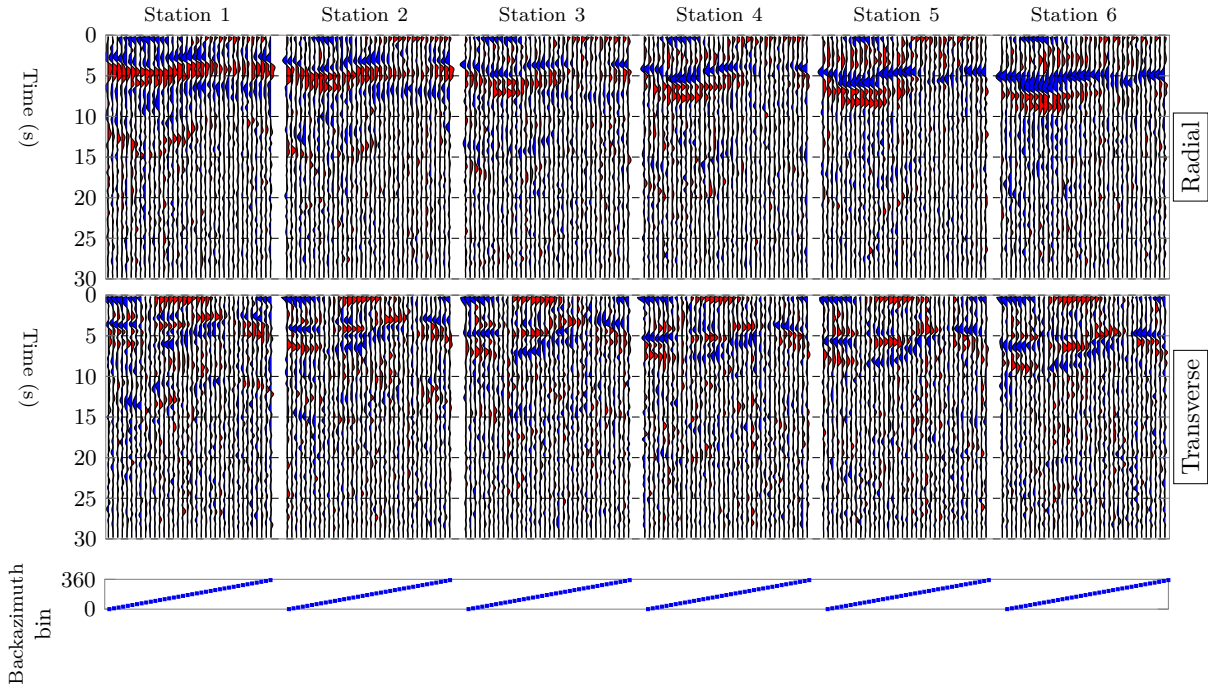


Figure 7: Linear stacked RFs for all stations (Synthetic experiment Model 2). All RFs are from same epicentral bin ($40^\circ - 50^\circ$), across all backazimuth bins. Note that there is no P arrival at $t = 0$ due to the *mean-subtraction*.

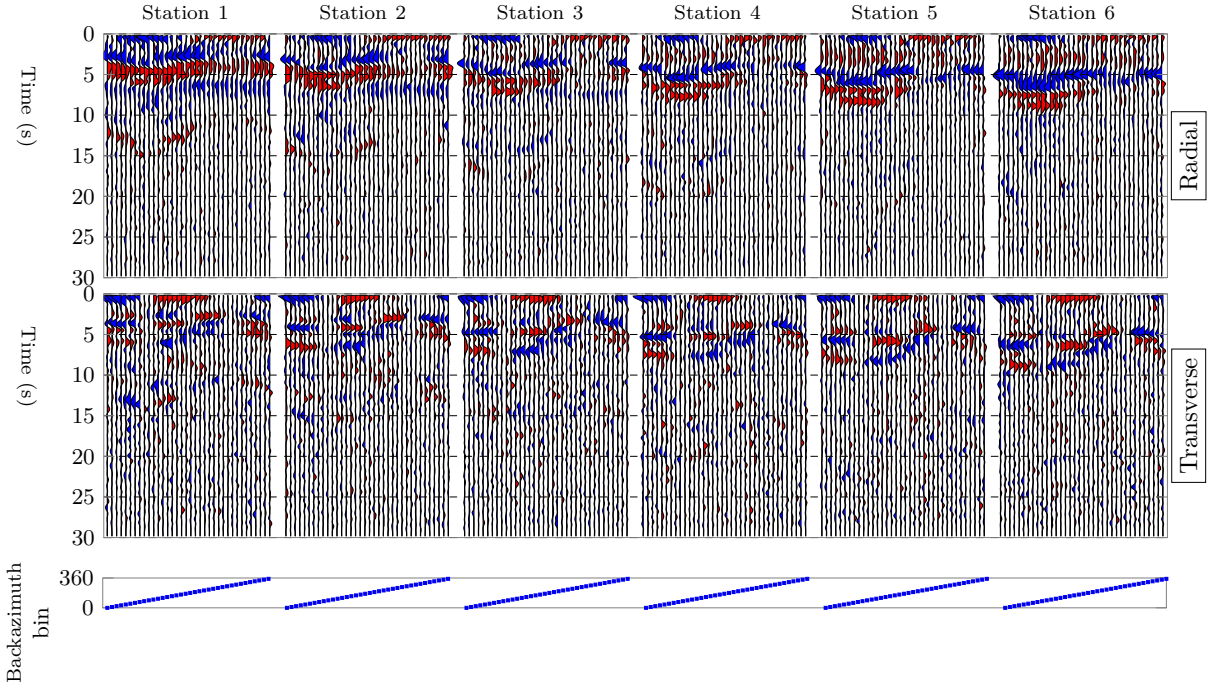


Figure 8: Bin-wise phase-weighted-stacked (PWS) RFs for all stations (Synthetic experiment Model 2). $\beta = 0.8$. All RFs are from same epicentral bin ($40^\circ - 50^\circ$), across all backazimuth bins. Note that there is no P arrival at $t = 0$ due to the *mean-subtraction*.

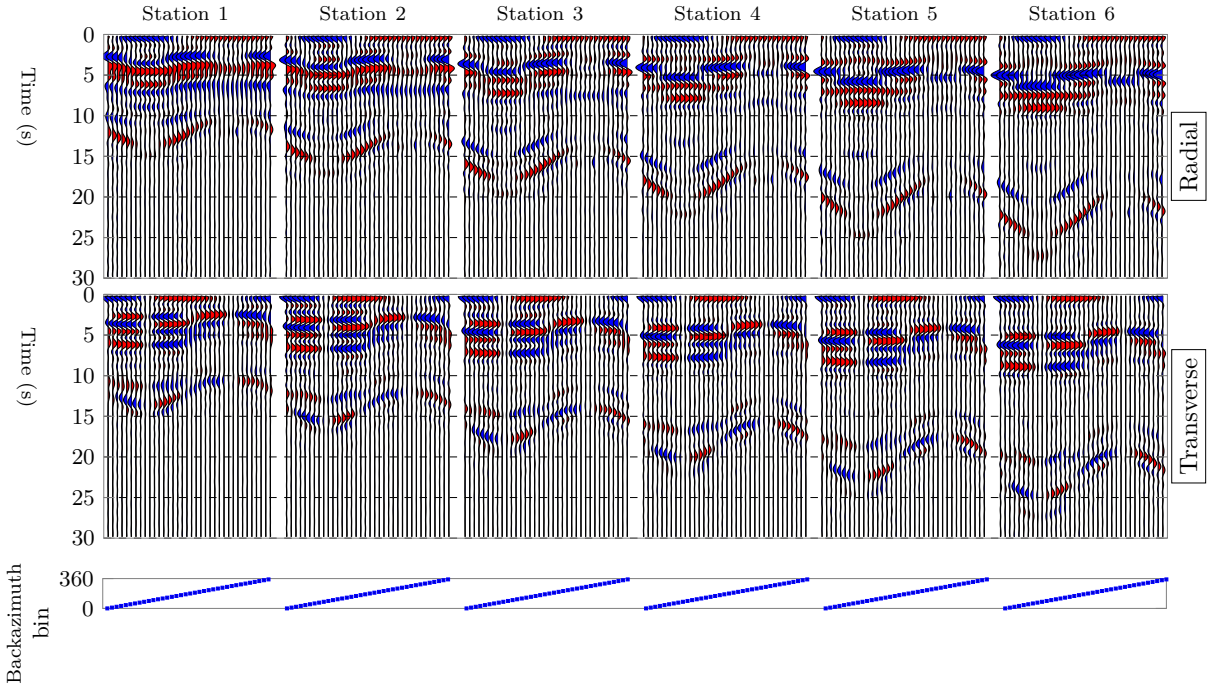


Figure 9: True RFs for all stations (Synthetic experiment Model 2). All RFs are from same epicentral bin ($40^\circ - 50^\circ$), across all backazimuth bins. Note that there is no P arrival at $t = 0$ due to the *mean-subtraction*.

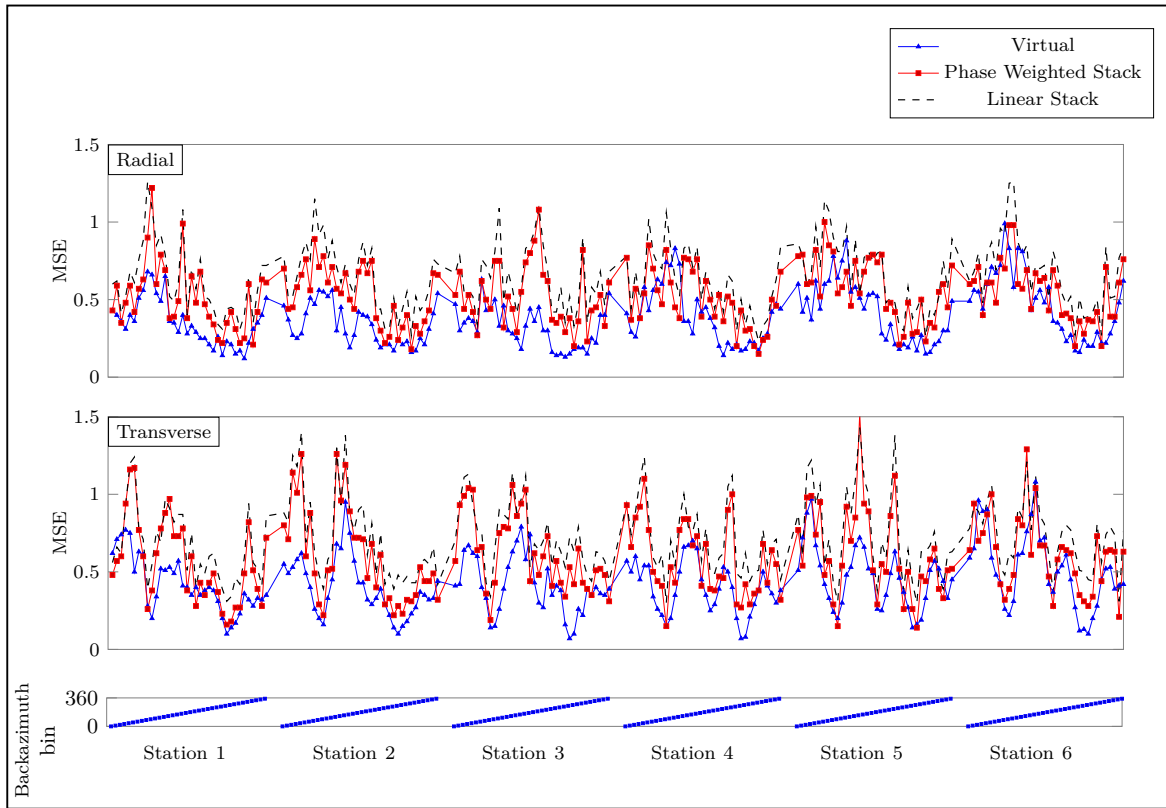


Figure 10: Mean Square Error (MSE) of virtual (Fig. 6), linear stacked (Fig. 7) and phase-weighted-stacked (Fig. 8) RFs w.r.t corresponding true RFs (Fig. 9) for all stations (Model 2).

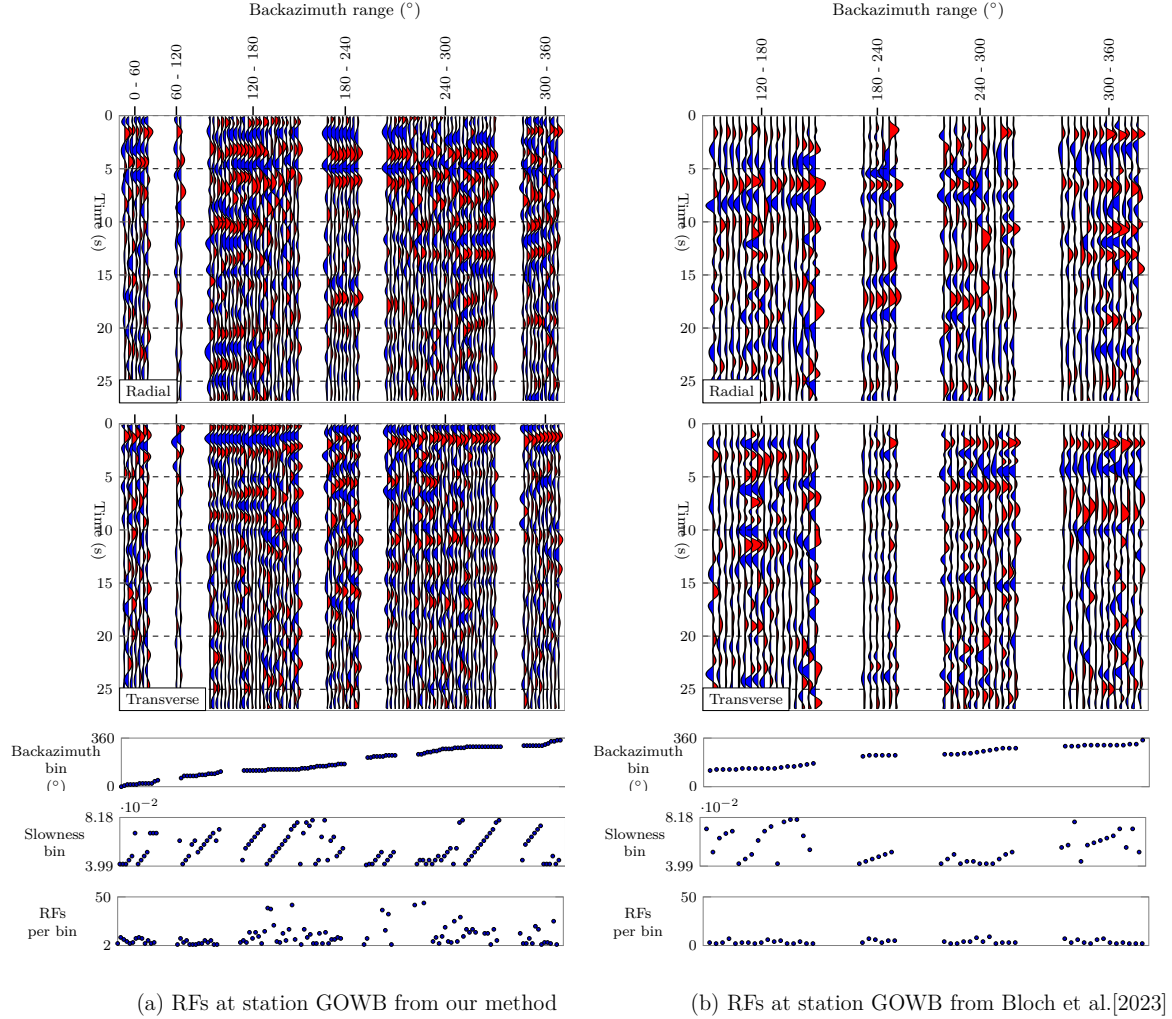


Figure 11: Radial and transverse RFs at station GOWB from our method and *Bloch et al. [2023]* demonstrating the correspondence. RFs are sorted by increasing backazimuth and slowness. Groups of RFs within a 60° backazimuth range are shown together for comparative convenience. Our method yields a larger coverage of RFs in terms of backazimuth, relative to *Bloch et al. [2023]*. Notably, the converted S-waves between 0 and 10 s are more distinct in (a) as opposed to (b).

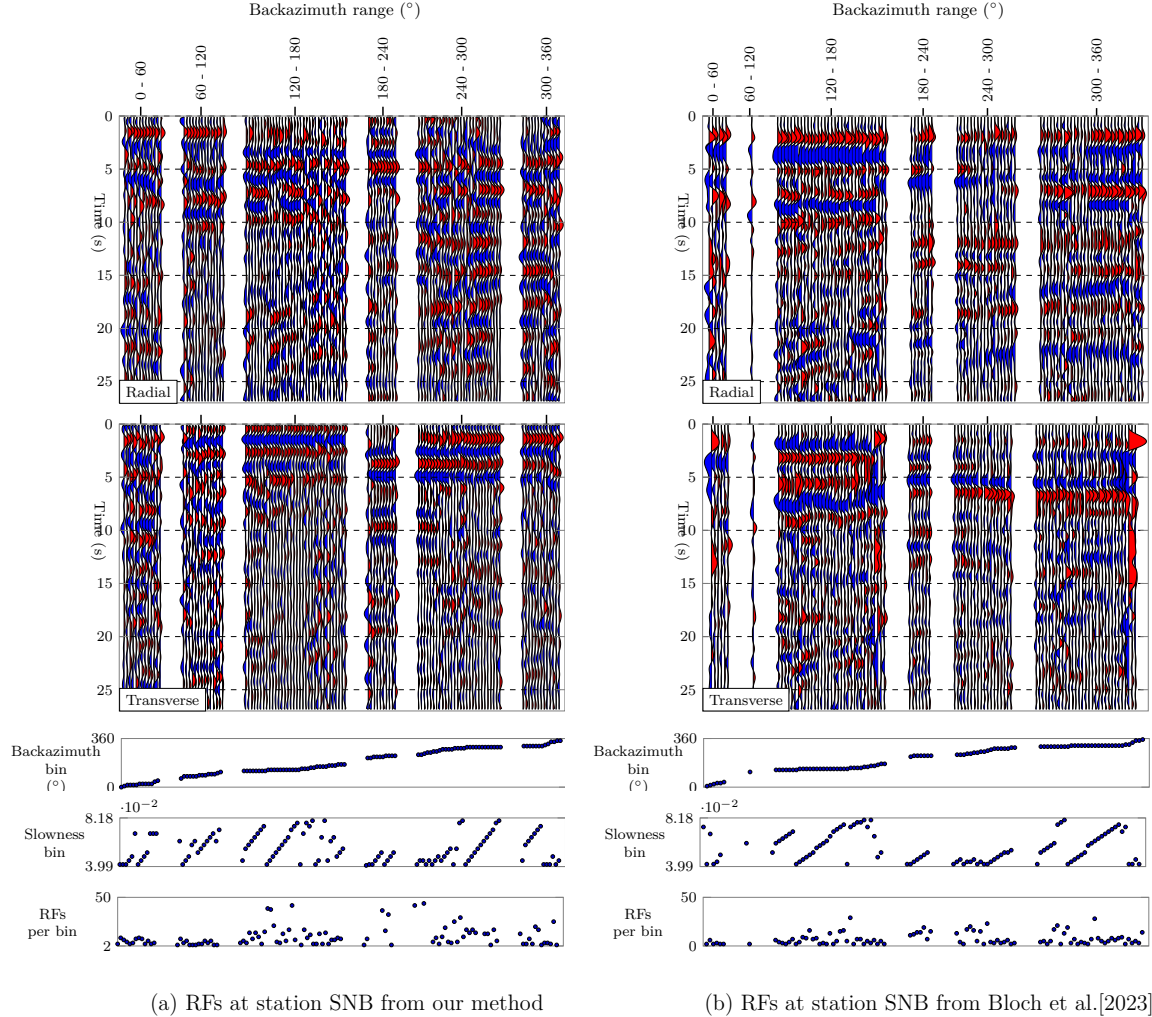


Figure 12: Radial and transverse RFs at station SNB from our method and *Bloch et al. [2023]* demonstrating the correspondence. The RFs are organized by ascending backazimuth and slowness. For ease of comparison, RFs within a 60° backazimuth range are grouped together. Our method generates RFs for the backazimuth range 60°–120°, which are missing in *Bloch et al. [2023]*, featuring distinct converted S-waves. These converted S-waves are more prominently visible between 0 to 10 s in (a) compared to (b). Additionally, notable polarity reversals in transverse RFs are observed between 0 to 5 s, approximately at backazimuth 60° and 180°, more so in (a).